Myosin II proteins are required for organization of calcium-induced actin networks upstream of mitochondrial division

Frieda Kage[a], Miguel Vicente-Manzanares[b], Brennan C. McEwan[a,c], Arminja N. Kettenbach[a,c], and Henry N. Higgs[a,*]

[a]Department of Biochemistry and Cell Biology and [c]Program in Cancer Biology, Geisel School of Medicine at Dartmouth College, Dartmouth College, Hanover, NH 03755; [b]Centro de Investigacion del Cancer/Instituto de Biologia Molecular y Celular del Cancer, Universidad de Salamanca, 37007 Salamanca, Spain

ABSTRACT **The formin INF2 polymerizes a calcium-activated cytoplasmic network of actin filaments, which we refer to as calcium-induced actin polymerization (CIA). CIA plays important roles in multiple cellular processes, including mitochondrial dynamics and vesicle transport. Here, we show that nonmuscle myosin II (NMII) is activated within 60 s of calcium stimulation and rapidly recruited to the CIA network. Knockout of any individual NMII in U2OS cells affects the organization of the CIA network, as well as three downstream effects: endoplasmic-reticulum-to-mitochondrial calcium transfer, mitochondrial Drp1 recruitment, and mitochondrial division. Interestingly, while NMIIC is the least abundant NMII in U2OS cells (>200-fold less than NMIIA and >10-fold less than NMIIB), its knockout is equally deleterious to CIA. On the basis of these results, we propose that myosin II filaments containing all three NMII heavy chains exert organizational and contractile roles in the CIA network. In addition, NMIIA knockout causes a significant decrease in myosin regulatory light chain levels, which might have additional effects.**

Monitoring Editor
Laurent Blanchoin
CEA Grenoble

Received: Jan 12, 2022
Revised: Mar 10, 2022
Accepted: Apr 5, 2022

INTRODUCTION

Increased cytoplasmic calcium causes a rapid increase in actin filaments throughout the cytosol (Ji *et al.*, 2015; Shao *et al.*, 2015; Wales *et al.*, 2016; Chakrabarti *et al.*, 2018), a process we call calcium-induced actin polymerization (CIA). Many stimuli can trigger CIA, including those that induce calcium entry from the extracellular space and those that trigger calcium release from the endoplasmic reticulum (ER). CIA is rapid and generally transient, peaking within 2 min and depolymerizing entirely within 5 min.

The key polymerization factor for CIA is the formin INF2. Two splice variants of INF2 exist, with different cellular localizations. INF2-CAAX is stably bound to the cytoplasmic face of the ER (Chhabra *et al.*, 2009), while INF2-nonCAAX is cytosolic (Ramabhadran *et al.*, 2011). Both splice variants trigger extensive actin polymerization throughout the cytosol, with INF2-CAAX polymerized filaments originating from the ER. The filaments generated by the two splice variants have different functions. CIA through INF2-CAAX impacts mitochondrial function in three ways: 1) it stimulates ER-to-mitochondrial calcium transfer, 2) it stimulates mitochondrial recruitment of the dynamin GTPase Drp1, and 3) it stimulates mitochondrial division (Korobova *et al.*, 2013; Ji *et al.*, 2015; Chakrabarti *et al.*, 2018). CIA through INF2-nonCAAX has less defined roles but acts in directional membrane transport (Andrés-Delgado *et al.*, 2010; Madrid *et al.*, 2010; Lamm *et al.*, 2018). INF2 also has been shown to polymerize actin filaments in the nucleus (Wang *et al.*, 2019) and to take part in calcium-stimulated epithelial cell extrusion (Takeuchi *et al.*, 2020). In addition, INF2 can bind microtubules and can alter tubulin acetylation (Gaillard *et al.*, 2011; Bartolini *et al.*, 2016; Fernández-Barrera *et al.*, 2018).

The importance of CIA to cellular physiology is suggested by the linkage of INF2 mutations to two diseases: focal segmental glomerulosclerosis (FSGS), a kidney disease; and Charcot–Marie–Tooth disease (CMTD), a peripheral neuropathy (Brown *et al.*, 2010; Boyer *et al.*, 2011; Labat-de-Hoz and Alonso, 2020). In both cases, long polarized cells are affected, podocytes for FSGS and Schwann cells

This article was published online ahead of print in MBoC in Press (http://www.molbiolcell.org/cgi/doi/10.1091/mbc.E22-01-0005) on April 15, 2022.

*Address correspondence to: Henry N. Higgs (henry.higgs@dartmouth.edu).

Abbreviation used: CIA, calcium-induced actin polymerization.

or neurons for CMTD. Disease-linked INF2 mutations are dominant and are likely to result in dysregulated actin polymerization (Mu *et al.*, 2019; Bayraktar *et al.*, 2020).

Other proteins are likely needed to organize INF2-polymerized filaments during CIA. A specific splice variant of the WH2 domain–containing protein Spire1 is tightly bound to the outer mitochondrial membrane and has been shown to function with INF2-CAAX (Manor *et al.*, 2015). The actin bundling protein fascin also has been shown to be important for INF2-dependent effects on mitochondria (Lin *et al.*, 2019). Finally, members of the myosin II family play a role in INF2 function. Both inhibition of myosin II by small molecules and knockdown (KD) of myosin IIA or myosin IIB heavy chains decrease INF2-mediated effects on mitochondrial division (Korobova *et al.*, 2014). These results suggest that myosin II activity is needed for cellular INF2 functions.

However, many aspects of myosin II function in CIA are unclear. First, it is unclear whether myosin II is necessary for the rapid changes to actin and mitochondria that occur upon acute calcium increase. Second, it is unclear as to which myosin II protein is involved in CIA. There are three nonmuscle myosin II (NMII) heavy chains in mammals, encoded by distinct genes: myosin IIA (NMIIA, *myh9* gene), myosin IIB (NMIIB, *myh10*), and myosin IIC (NMIIC, *myh14*). NMIIA and NMIIB have been extensively studied in several contexts, including cell migration (Vicente-Manzanares *et al.*, 2007; Fenix *et al.*, 2016; Beach *et al.*, 2017; Hu *et al.*, 2017; Shutova *et al.*, 2017) and cortical actin dynamics (Taneja and Burnette, 2019; Yamamoto *et al.*, 2019; Taneja *et al.*, 2020). Much less is known about NMIIC's cellular functions, which is expressed at lower levels than NMIIA or NMIIB in most tissues and cell types (Ma *et al.*, 2010). One recent study, however, suggests a function for NMIIC in mitochondrial dynamics (Almutawa *et al.*, 2019).

Complicating the elucidation of cellular myosin II function is the fact that the three nonmuscle heavy chains can potentially hetero-oligomerize. The myosin II heavy chain is a constitutive dimer, which is considered the basal oligomeric state. This dimer further oligomerizes into large multimeric structures called "filaments" of heavy chains, with motor heads oriented in opposite directions. All three nonmuscle myosins can form filaments, with NMIIA and NMIIB assembling into structures containing ~30 heavy chains and NMIIC assembling into structures containing ~14 heavy chains (Billington *et al.*, 2013). The three NMII heavy chains have also been shown to hetero-oligomerize in cells (Beach *et al.*, 2014).

In addition to the NMII heavy chains, there are also two light chains that are obligatorily bound to the neck region of each heavy chain (Sellers and Heissler, 2019): the essential light chain (ELC) and the myosin regulatory light chain (MRLC). RLC is mandatory for NMII hexamer assembly, whereas ELC is not, but it is required for the hexamer to be contractile (Xu *et al.*, 2001). Regulation of NMII occurs through MRLC phosphorylation by several kinases, with phosphorylation on S19 releasing the folded dimer into an oligomerization-competent state and allowing ATPase activity (Sellers and Heissler, 2019). Other phosphorylation events on MRLC and other subunits can have additional regulatory effects (Dulyaninova and Bresnick, 2013; Aguilar-Cuenca *et al.*, 2020). While there are three main MRLCs expressed in nonmuscle cells, MYL9, MYL12A, and MYL12B (Heissler and Sellers, 2015), it is unknown whether any of them display a preference for the NMIIA, NMIIB, or NMIIC heavy chains.

This paper addresses the function of NMII in CIA. Although present at much lower levels than NMIIA or NMIIB in U2OS cells, NMIIIC has an equal role in CIA and its downstream effects. The effect on CIA is not on the polymerization of actin, which is mediated by the formin INF2, but on the organization of these filaments into a network. All NMII paralogues can enrich in the CIA network, which might suggest that the functional NMII oligomer contains all three heavy chains that can organize and exert force on the network with functional consequences for mitochondrial organization and dynamics.

RESULTS

Myosin II is activated on the same timescale as CIA

We assessed the phosphorylation state of MRLC upon treatment of U2OS cells with ionomycin, a calcium ionophore that causes a rapid and transient increase in cytoplasmic calcium and triggers CIA through INF2 activation (Chakrabarti *et al.*, 2018). As observed previously, CIA occurs throughout the cytoplasm within 1 min of ionomycin treatment (Figure 1A). MRLC phosphorylation also increases rapidly, with a ~2.75-fold increase within 1 min (Figure 1, B and C). Phosphorylated MRLC levels remain elevated for at least 10 min poststimulation, while CIA terminates within 3 min (Figure 1C). By immunofluorescence microscopy, puncta of phosphorylated MRLC colocalize with the CIA network upon 45 s of ionomycin treatment (Figure 1D). Similar rapid MRLC phosphorylation occurs upon histamine stimulation (Figure 1E), which triggers calcium release from the ER and stimulates CIA on the same timescale (Chakrabarti *et al.*, 2018). HeLa cells also display rapid MRLC phosphorylation upon cytoplasmic calcium increase (Supplemental Figure S1A). These results suggest that rapid myosin II activation could contribute to CIA.

NMIIA is the most abundant heavy chain in U2OS cells

Before asking which of the three nonmuscle myosin II heavy chains might contribute to CIA, we first determined which NMII heavy chains are expressed in U2OS cells. The relative protein levels of NMIIA, B, and C have been compared in a number of tissues and cell types (Golomb *et al.*, 2004; Ma *et al.*, 2010), but not in a manner that provides per-cell concentrations. To establish NMII heavy chain concentrations, we used purified NMIIA, B, and C (Supplemental Figure S1B) as standards for quantitative Western blotting. Commercially available antibodies display high specificity to their designated NMII heavy chain (Supplemental Figure S1C). Using these antibodies on extracts of defined cell numbers, and with the purified standards as internal controls for protein concentration (Supplemental Figure S1D), we determined that U2OS cells possess approximately 2.0×10^7, 1.3×10^6, and 9.2×10^4 molecules/cell of NMIIA, B, and C, respectively (Figure 2, A and B). Using a cellular cytoplasmic volume of 3.14 pl/cell, calculated from morphometric analysis of whole cell and organellar volumes of Cos7 cells (Valm *et al.*, 2017; Mu *et al.*, 2020), we estimate cytoplasmic myosin II heavy chain monomer concentrations at 10.8, 0.68, and 0.049 μM for NMIIA, B, and C, respectively. From these concentrations, the molar ratio of NMIIA:NMIIB:NMIIC in U2OS cells is 220:14:1. In these same U2OS extracts, we used similar quantitative Western blotting techniques to determine the concentration of actin to be 1.2×10^8 molecules/cell, corresponding to 65.1 μM (Figure 2, A and B, and Supplemental Figure S1, E and F).

We also used a proteomic approach for assessing the ratios of the three NMIIs, quantifying numbers of unique peptides, and obtained values of 86:5:1 NMIIA:NMIIB:NMIIC (Supplemental Figure S1G; Supplemental Table S1). Taken together, these results show that NMIIA is by far the most abundant NMII in U2OS cells, with NMIIB and NMIIC being ~10-fold and ~100-fold less abundant, respectively.

NMIIA knockout affects MRLC levels, stress fiber morphology, and focal adhesion size

To assess the roles of all three NMII heavy chains in CIA, we used CRISPR-mediated knockouts (KOs) in U2OS cells. These KOs result

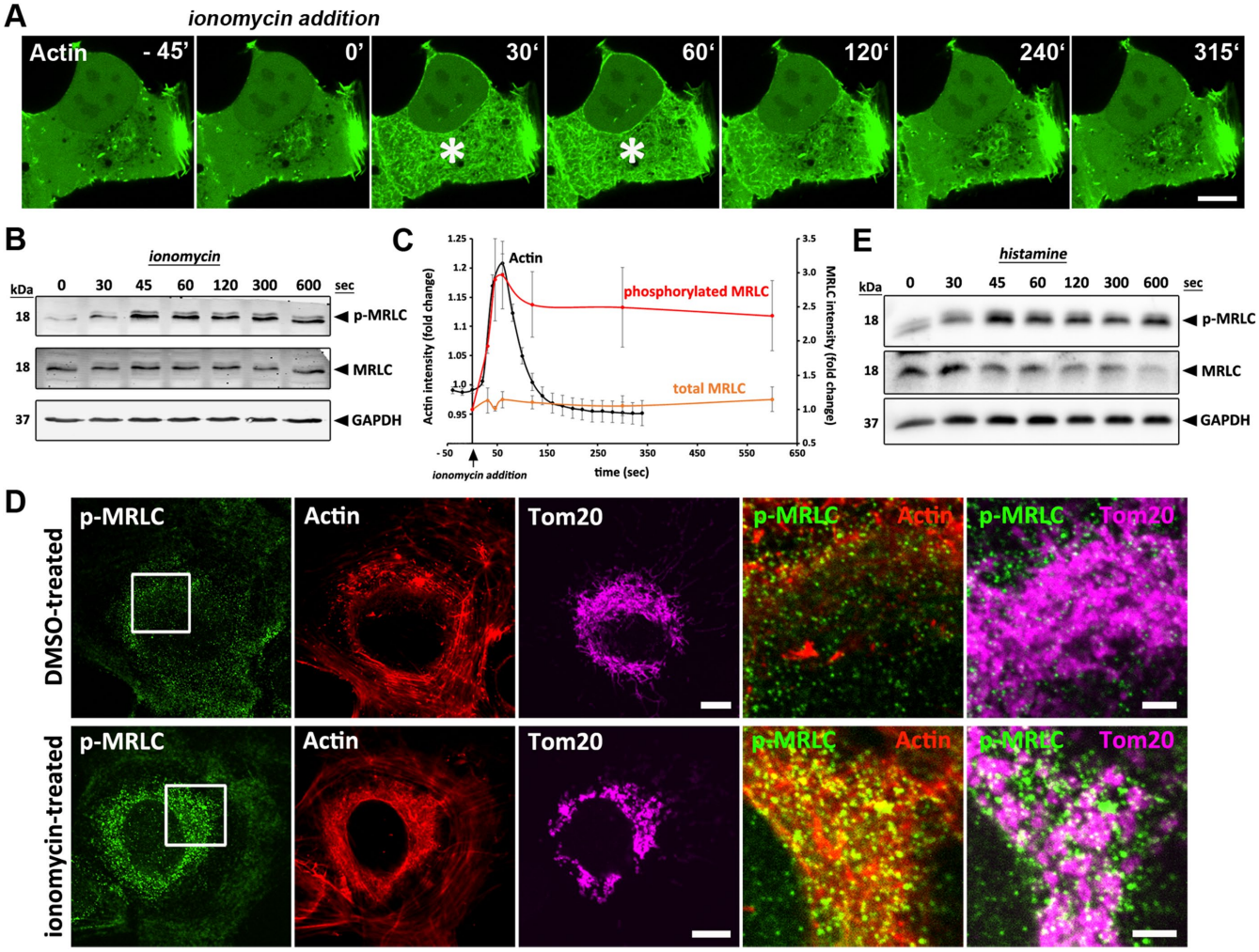

FIGURE 1: Increased cytoplasmic calcium triggers rapid myosin II activation. (A) Time-lapse montage of U2OS cell transfected with GFP-F-tractin and stimulated with ionomycin for the indicated times (seconds). Medial cell section imaged. Asterisks highlight the cytoplasmic CIA network. Bar is 10 μm. (B) Western blots of U2OS cell extracts after the indicated times of ionomycin treatment. (C) Plot of time course for changes in cytoplasmic actin polymerization as well as phosphorylated MRLC and total MRLC changes after ionomycin addition in U2OS cells. Error bars are SEM. (D) Images of fixed U2OS cells stained for phosphorylated MRLC, actin filaments (TRITC-phalloidin), and mitochondria (Tom20) after 45 s stimulation with DMSO (top) or ionomycin (bottom). Images at right are color merged zooms of boxed regions. Bar is 10 μm in overview images and 3 μm in zooms. (E) Western blots of U2OS cell extracts after the indicated times of histamine treatment.

in apparent full ablation of the targeted myosin in multiple independent clones (Figure 2C). The loss of one NMII heavy chain does not change expression of the other two heavy chains (Figure 2D). Interestingly, NMIIA KO results in an 83 and 80% depletion of total MRLC and phospho-MRLC, respectively, in all three clones tested (Figure 2, E and F). In contrast, neither NMIIB nor NMIIC KO causes a significant change in MRLC levels (Figure 2, E and F). Similar effects on MRLC expression occur upon NMIIA KD by small interfering RNA (siRNA) (Supplemental Figure S2A).

One concern is that the antibodies used to detect MRLC recognize only a subset of MRLC proteins. From the Human Protein Atlas, the three predominant MRLCs expressed in U2OS cells are Myl12B, Myl12A, and Myl9. Using plasmids for FLAG-tagged Myl12A and Myl9, we show that both the anti-MRLC and anti–phospho-MRLC antibodies used here recognize both proteins, but not the Myl6 essential light chain (Supplemental Figure S2B). In view of the role of MRLC in regulation of all three NMII heavy chains, as well as its potential role in regulating other myosins (Heissler and Sellers, 2015), the possibility of indirect effects of NMIIA KO through MRLC reduction should be considered for the cellular effects described below.

NMIIA deletion has been shown to compromise stress fiber and focal adhesion distribution (Even-Ram *et al.*, 2007; Vicente-Manzanares *et al.*, 2007; Chang and Kumar, 2015; Kuragano *et al.*, 2018), most recently in U2OS cells described by Weißenbruch *et al.* (2021). We find similar effects in our CRISPR KO lines. Ventral stress fibers are normally linear structures with little noticeable curvature. In contrast, the ventral stress fibers in >75% of NMIIA KO cells are "wavy" and appear less bundled (Figure 3, A and B). In addition, both the number and size of focal adhesions decrease in NMIIA KO cells (Figure 3, C–E). Neither effect is observed in NMIIB KO cells. In NMIIC KO cells a modest but statistically significant reduction in focal adhesion numbers is measured.

All three NMII KOs affect CIA network morphology

As NMII activation through calcium occurs on a timescale similar to that of CIA, and endogenous MRLC associates with the CIA network,

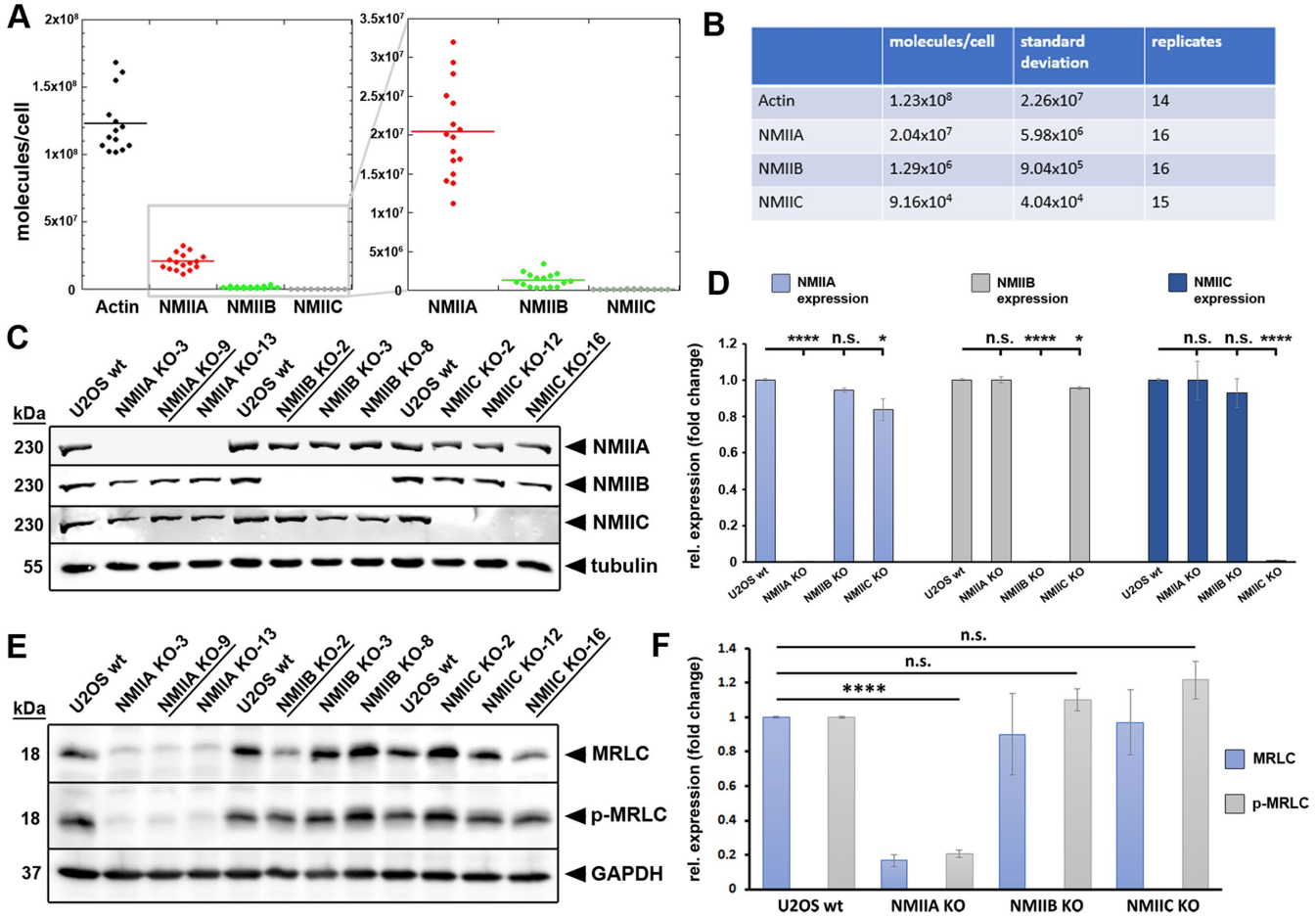

	molecules/cell	standard deviation	replicates
Actin	$1.23x10^8$	$2.26x10^7$	14
NMIIA	$2.04x10^7$	$5.98x10^6$	16
NMIIB	$1.29x10^6$	$9.04x10^5$	16
NMIIC	$9.16x10^4$	$4.04x10^4$	15

FIGURE 2: Myosin IIA deletion results in depletion of myosin regulatory light chain. (A) Plot of concentrations of actin, NMIIA, NMIIB, and NMIIC in U2OS cells. Zoom (gray box) of NMII data points alone on the right. See Supplemental Figure S1 for Western blots and quantification. (B) Table of mean protein concentrations in U2OS cells. (C) Western blots of NMII KO U2OS cell lines, examining NMIIA, NMIIB, and NMIIC levels in three independent clones for each KO. Tubulin serves as loading control. Underlined clones were used in further investigation. (D) Plot of protein levels from data in panel C, averaging levels from independent clones. Unpaired *t* test with *p* values as follows: >0.05 = not significant (n.s.), <0.0001 (****), and ≤0.05 (*). (E) Western blots probing for MRLC and phospho-MRLC in NMII KO U2OS cell lines. GAPDH serves as loading control. (F) Plot of protein levels from data in panel E, averaging levels from independent clones. Unpaired *t* test with *p* values as follows: >0.05 = not significant (n.s.) and <0.0001 (****).

we next investigated CIA in the individual NMII KO lines. We used a fixed-cell assay, in which CIA is assessed after 45 s of ionomycin stimulation by measuring mean actin filament intensity in perinuclear regions of medial focal planes, devoid of signal contribution from stress fibers and cortical actin. All three KOs display reductions in CIA, to 66, 74, and 56% of the control response for NMIIA, B, and C, respectively (Figure 4, A and B). Visual assessment of the images shows that a "filamentous" pattern is still present, but at reduced apparent density (Figure 4A). This effect contrasts with that of INF2 KD, in which CIA is entirely absent, indistinguishable from the dimethyl sulfoxide (DMSO) control (Figure 4, A and B), similar to past results (Chakrabarti *et al.*, 2018; Fung *et al.*, 2019). U2OS cells express both INF2-nonCAAX and INF2-CAAX, the former predominating (Ramabhadran *et al.*, 2011), but both isoforms are capable of CIA assembly (Chakrabarti *et al.*, 2018).

To analyze the kinetics of CIA, we used live-cell monitoring of actin filament intensity with GFP-F-tractin. For all three KOs, the peak intensity of the actin response to ionomycin is reduced and the time for maximal response is slightly delayed, but the attenuation of the response is not altered (Figure 4, C–E). Similar to the fixed-cell experiment, visual inspection of the actin network at peak stimulation suggests that bundled filaments are still present, but at reduced density (Figure 4C).

One possibility is that prolonged lack of NMII affects CIA indirectly. To check the effect of more acute NMII inhibition on CIA, we pretreated wild-type (WT) HeLa cells for 1 h with blebbistatin (Limouze *et al.*, 2004; Rauscher *et al.*, 2018) and then used the fixed-cell CIA assay at 45 s ionomycin stimulation. Blebbistatin reduces actin filament intensity by 44%, similar to the effect of NMII KOs (Supplemental Figure S3, A and B). Because this effect on CIA is observed in U2OS and HeLa cells, it indicates a general rather than a cell type–specific role for NMII members in CIA. Another possibility for an indirect effect is that NMII inhibition affects calcium release from the ER, which we have previously shown to mediate CIA (Chakrabarti *et al.*, 2018). We therefore tested whether NMII KO affects ER calcium release. By live-cell imaging of an ER-specific calcium sensor, none of the KO lines show altered ER calcium release (Supplemental Figure S3, C–E).

We also used a biochemical approach to assess NMII KO effects on CIA, whereby we rapidly extracted cells in buffer containing both

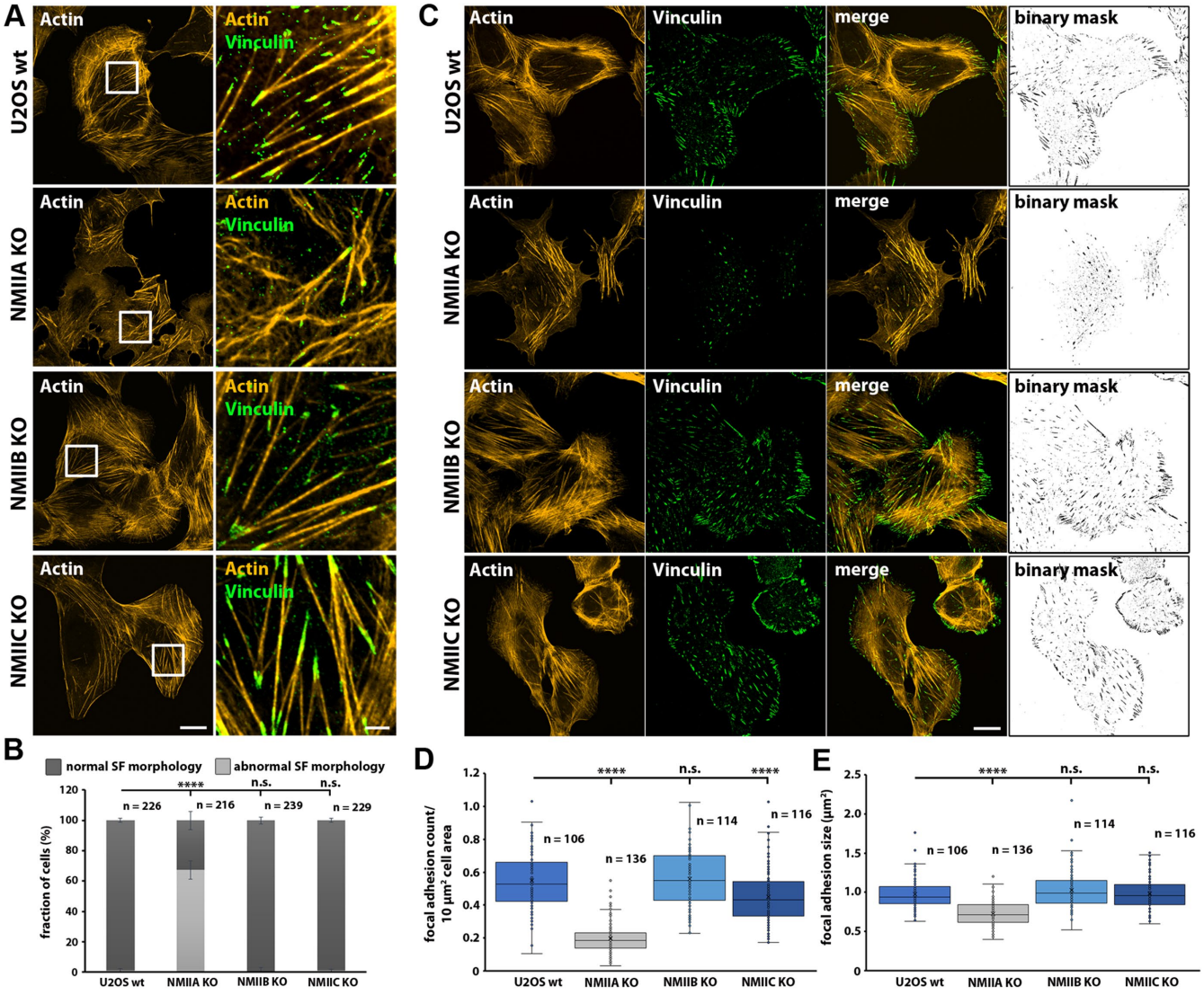

FIGURE 3: Myosin IIA deletion results in defects in stress fibers and focal adhesions in U2OS cells. (A) Fixed-cell images of WT and NMII KO cell lines stained for actin filaments (TRITC-phalloidin) and vinculin. Images at right are zooms of boxed regions. Bar is 20 µm in overview images and 3 µm in insets. (B) Plot of cells possessing "normal" (straight) ventral stress fibers vs. "abnormal" (wavy) stress fibers. Data obtained from three independent experiments. Error bars are SEM. Unpaired *t* test: *p* values for NMIIA KO < 0.0001 (****), NMIIB KO = 0.92 (n.s.), and NMIIC KO = 0.99 (n.s.). (C) Fixed-cell images of WT and NMII KO cell lines, focusing on focal adhesion abundance and morphology (vinculin staining). Binary masks used for quantifications in D and E. Bar is 20 µm. (D) Plot of focal adhesion density. Unpaired *t* test: *p* values for NMIIA KO < 0.0001 (****), NMIIB KO = 0.7 (n.s.), and NMIIC KO < 0.0001 (****). (E) Plot of focal adhesion size. Unpaired *t* test: *p* values for NMIIA KO < 0.0001 (****), NMIIB KO = 0.07 (n.s.), and NMIIC KO = 0.72 (n.s.).

phalloidin (to prevent depolymerization of existing filaments) and latrunculin A (LatA) (to prevent new polymerization after extraction) and then centrifuged the lysate to pellet actin filaments but not actin monomers. We then used Western blotting to obtain a ratio for actin intensity in the pellet versus supernatant. In unstimulated control cells, the pellet:sup ratio is 0.82 ± 0.16, whereas ionomycin treatment shifts this ratio to 2.27 ± 0.42, indicative of increased actin polymerization. As a negative control, LatA pretreatment for 20 min followed by ionomycin stimulation before extraction results in a ratio of 0.14 ± 0.01 (Figure 5, A–C).

Pellet:sup ratios for NMIIA, NMIIB, and NMIIC KOs in both the unstimulated and ionomycin-stimulated samples are similar to those of control cells (Figure 5, A–C). In contrast, INF2 KO cells display actin ratios similar to those of control cells in both unstimulated and ionomycin-stimulated conditions, demonstrating that the ionomycin-stimulated actin increase in the pellet is clearly dependent on INF2's polymerization activity. These results suggest that NMII does not decrease actin polymer levels in CIA, a result that differs from the quantification of fixed-cell images (Figure 4, A and B).

NMII is enriched on CIA filaments

If NMII plays a role in the organization of the CIA network, it should be present on this structure. Using the cellular actin pelleting assay, we examined the distribution of NMII upon ionomycin stimulation. All three NMII heavy chains increase in the pellet of ionomycin-treated cells relative to DMSO-treated cells (Figure 5D), suggesting their specific incorporation into the CIA network. As expected, INF2 is also increased in the pellet fraction of ionomycin-treated samples.

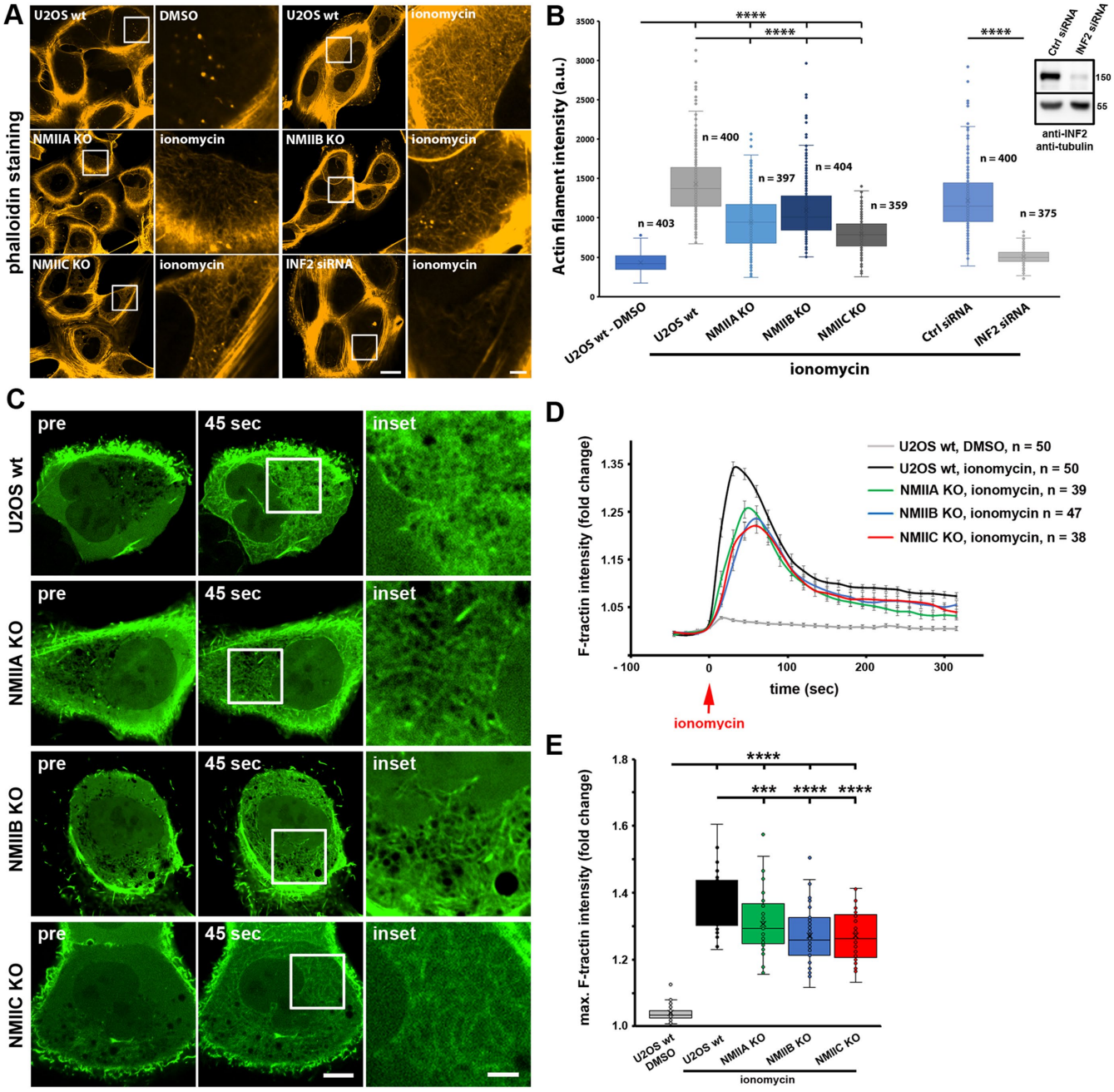

FIGURE 4: NMII deletion reduces the intensity of the actin network in CIA. (A) Fixed-cell imaging of WT and NMII KO U2OS cell lines for actin filaments (TRITC-phalloidin) in either unstimulated (DMSO) or ionomycin-stimulated (45 s) state, with zooms to the right denoting boxed regions of full-field views. INF2 KD cells also shown. Bar is 20 μm in overview images and 3 μm in insets. (B) Plot of actin filament intensity from fixed-cell images as in panel A. Western blot at right shows efficiency of INF2 KD. Unpaired *t* test: *p* values < 0.0001 (****) for all cell lines. (C) Live-cell imaging of WT and NMII KO U2OS cell lines for actin (GFP-F-tractin), both before (pre) and after (45 s) ionomycin treatment. Bar is 10 μm in overview images and 3 μm in insets. (D) Quantification of F-tractin intensity changes upon ionomycin stimulation for the indicated cell lines. Error bars are SEM. (E) Plot of maximal change in F-tractin levels from the data in panel D. Unpaired *t* test with *p* values < 0.0001 (****) and 0.0007 (***).

In contrast, neither Arp2/3 complex nor the actin cross-linker α-actinin 1 increases in the ionomycin-stimulated pellet (Figure 5D), demonstrating that NMII pellet enrichment is not simply caused by unspecific binding to actin. We have previously shown that Arp2/3 complex is not required for CIA (Fung *et al.*, 2019).

We also used immunofluorescence microscopy to examine NMII presence on the CIA network. For this staining, we modified our fixation procedure, because the anti-NMII antibodies proved to be ineffective after our standard glutaraldehyde fixation (see *Materials and Methods*), which preserves the CIA network best. The modified fixation procedure results in less complete preservation of the CIA network but is sufficient to assess NMII localization. All three NMII heavy chains display specific enrichment in the CIA network upon ionomycin treatment, while no NMII accumulation besides the

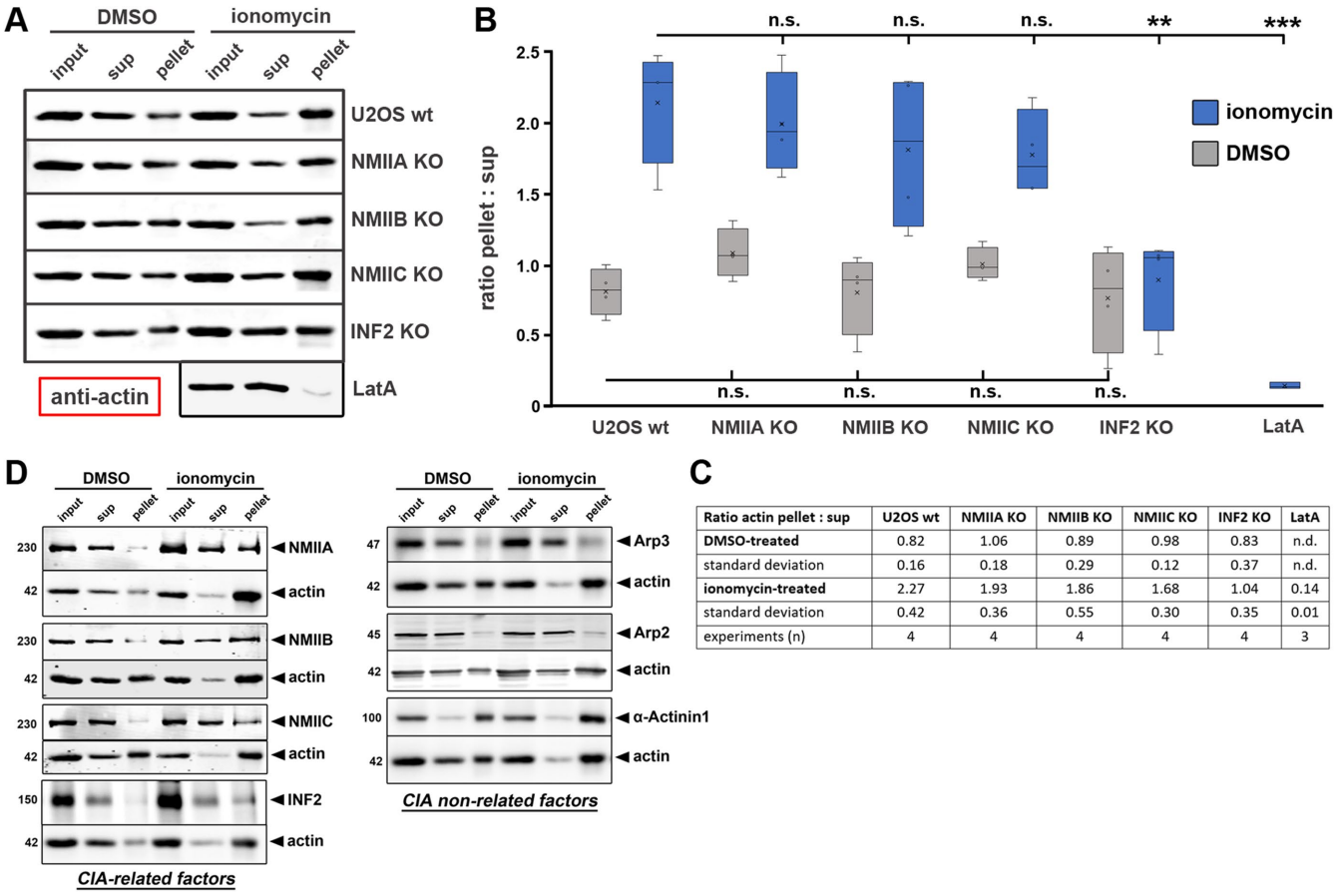

C

Ratio actin pellet : sup	U2OS wt	NMIIA KO	NMIIB KO	NMIIC KO	INF2 KO	LatA
DMSO-treated	0.82	1.06	0.89	0.98	0.83	n.d.
standard deviation	0.16	0.18	0.29	0.12	0.37	n.d.
ionomycin-treated	2.27	1.93	1.86	1.68	1.04	0.14
standard deviation	0.42	0.36	0.55	0.30	0.35	0.01
experiments (n)	4	4	4	4	4	3

FIGURE 5: NMII proteins incorporate into the CIA network. (A) Western blots of actin from experiments in which U2OS cells were stimulated with either DMSO or ionomycin for 45 s, extracted with nonionic detergent, and then separated into supernatant and pellet fractions by ultracentrifugation. For the LatA sample, cells were pretreated with 2 μM LatA 20 min before ionomycin treatment. (B) Ratio of actin in the pellet vs. supernatant for experiments in panel A (four replicates). Unpaired *t* test with *p* values > 0.05 considered not significant (n.s.), *p* values for ionomycin-treated INF2 KO = 0.0038 (**) and for LatA = 0.0005 (***). (C) Numerical data for panel B. n.d., not determined. (D) Western blots of several proteins in assays described in panel A, to determine whether their distribution changes upon ionomycin stimulation. Actin shown as a control for each protein (from the same blot as the protein of interest).

expected stress fiber localization is observed in DMSO-treated cells (Figure 6). Using the same procedure, we stained for endogenous tropomyosin 3 (Tpm3), which is present on actin structures, such as stress fibers, similarly to NMII. As opposed to NMII, tropomyosin 3 did not show a specific enrichment in the CIA network, demonstrating that NMII association with the network is not simply caused by indirect actin binding (Supplemental Figure S4).

We also tested GFP fusions of the respective NMII heavy chains, transfected into their corresponding KO U2OS cell line, selecting cells with low expression levels for analysis by fixed-cell microscopy. In unstimulated cells, NMII–GFP fusions are largely absent from the bulk cytoplasmic region but decorate stress fibers in a striated pattern (Supplemental Figure S5). In ionomycin-stimulated cells, however, all NMII–GFP fusions enrich as puncta on the CIA network, oftentimes surrounding mitochondria (Supplemental Figure S5).

NMII plays a role in mitochondrial morphology, CIA-induced mitochondrial calcium uptake, and mitochondrial division

We have shown that CIA is important for efficient ER-to-mitochondrial calcium transfer, with transfer being almost completely eliminated in INF2 KO or INF2 KD cells (Chakrabarti *et al.*, 2018). To test the roles of individual NMII heavy chains in this process, we monitored the change in fluorescence of the mitochondrial calcium probe mito-R-GECO in WT or NMII KO U2OS cells. All three NMII KO lines display decreased ionomycin-induced mitochondrial calcium uptake, with NMIIA and NMIIC KO being the most pronounced (Figure 7, A–C). This effect is not due to decreased release of calcium from the ER, which is similar to that of WT cells in all cases (Supplemental Figure S3, C–E).

We also used a panel of NMII inhibitors to test for a similar effect on ionomycin-induced mitochondrial calcium uptake. Blebbistatin causes a 40% decrease in peak mito-R-GECO fluorescence (Supplemental Figure S6, A–C). Similar effects occur using two inhibitors of MRLC phosphorylation, Y27632 (a Rho-kinase inhibitor) and ML-7 (a myosin light chain kinase inhibitor), with 28 and 37% decreases, respectively (Supplemental Figure S6, A–C). These results suggest that NMII plays a role in CIA-mediated mitochondrial calcium uptake. Because efficient calcium transfer from the ER to mitochondria requires these organelles to be in close proximity, we propose that NMII might contribute by F-actin contraction and/or stabilization of the CIA network at ER–mito contacts.

We also examined the effect of NMII KO on mitochondria morphology, using fixed cells stained for the outer mitochondrial membrane (OMM) protein Tom20. We first compared mitochondrial diameters in perinuclear and peripheral mitochondria, as mitochondrial diameter appeared to be different depending on the cellular

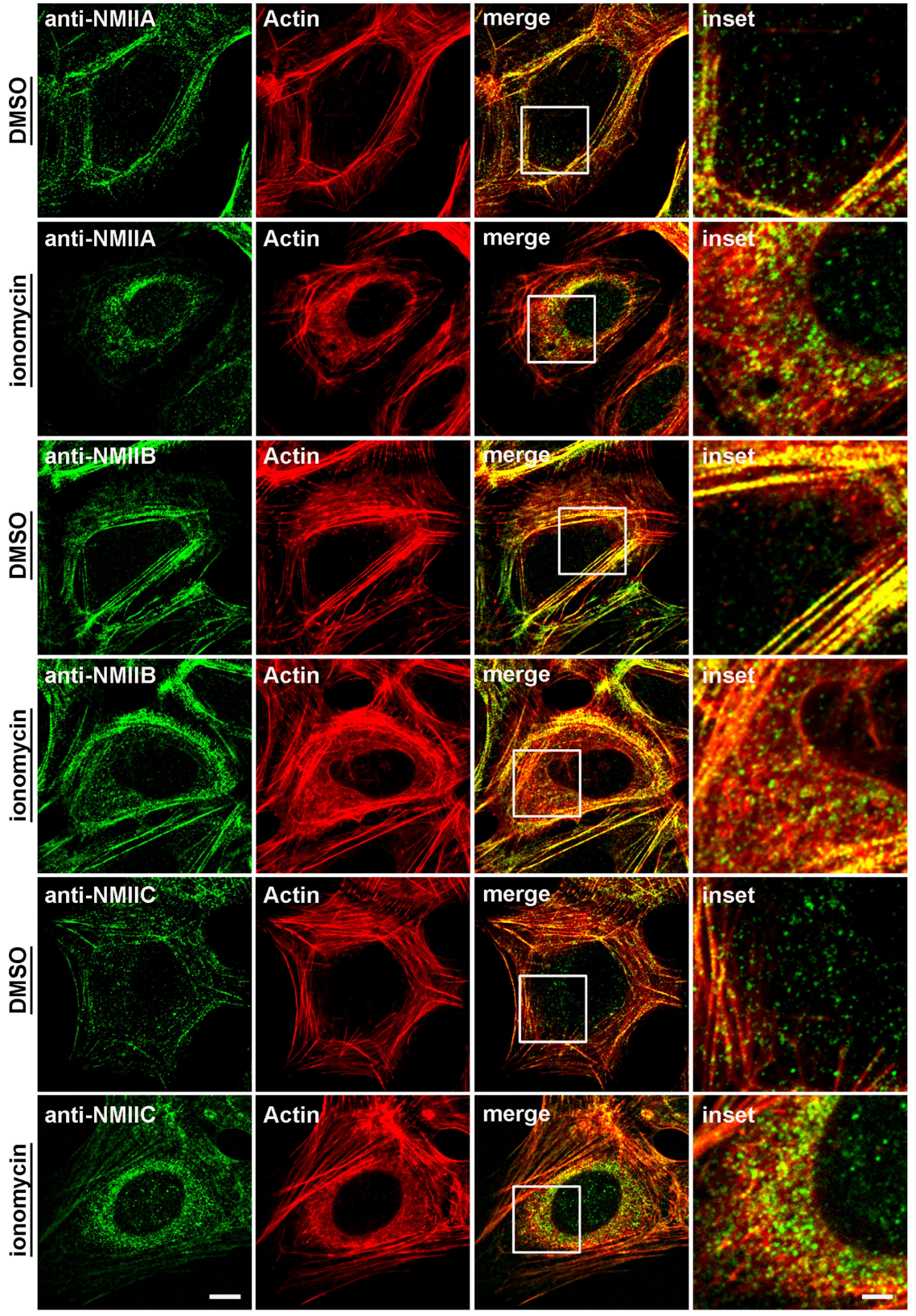

FIGURE 6: Enrichment of endogenous NMII heavy chains to CIA network. Immunofluorescence microscopy of U2OS cells that were first permeabilized for 1 min in the presence of TRITC-phalloidin to stabilize actin filaments and then fixed with PFA followed by anti-NMII staining. For each NMII, an example of control treatment (DMSO) and ionomycin treatment (45 s) is shown. Insets emphasize CIA network near the nucleus, where it is most prominent and where other actin-based structures are sparse. Scale bar is 10 μm in overview images and 3 μm in insets.

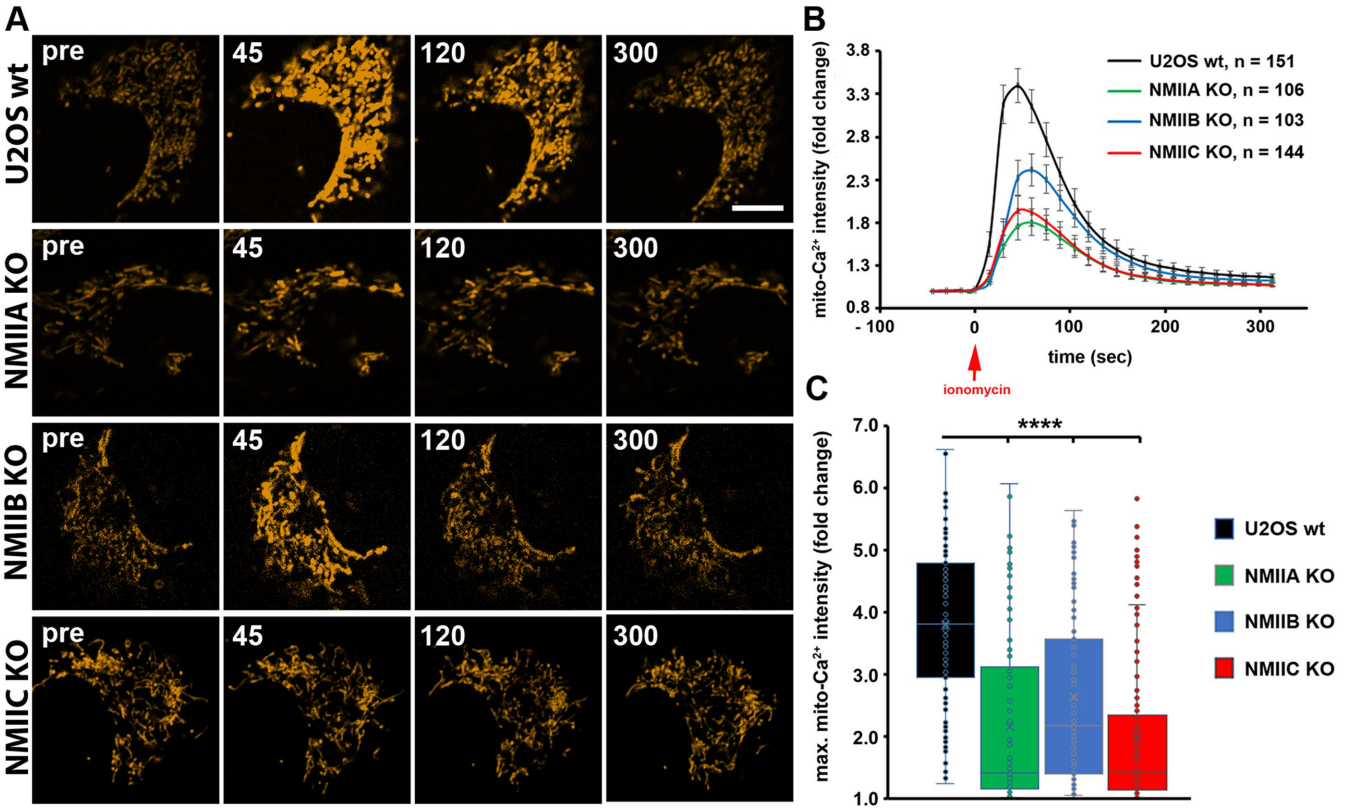

FIGURE 7: NMII KO inhibits CIA-stimulated mitochondrial calcium influx. (A) Live-cell imaging of WT or NMII KO U2OS cell lines transfected with the mito-R-GECO probe to monitor mitochondrial calcium levels. One time point before stimulation (pre) and three time points (in seconds) after ionomycin stimulation are shown. Bar is 10 μm. (B) Plot of mitochondrial calcium changes upon ionomycin stimulation for the indicated cell lines. Error bars are SEM. (C) Plot of maximal change in mitochondrial calcium levels from the data in panel B. Unpaired *t* test with *p* values < 0.0001 (****).

location and the respective myosin KO. One observation is that peripheral mitochondria (at least 10 μm away from the nucleus) are significantly "thinner" in NMIIB and NMIIC KO cells than in WT or NMIIA KOs, changing from 0.54 ± 0.07 μm in WT and 0.53 ± 0.06 μm in NMIIA KO cells to 0.43 ± 0.05 and 0.44 ± 0.05 μm in NMIIB and C KOs, respectively (Figure 8, A and B). A second observation is that perinuclear mitochondria (within a ~10 μm radius around the nucleus) are affected in different ways to peripheral mitochondria by NMII KO. For WT cells, perinuclear mitochondrial diameter (0.70 ± 0.09 μm) is significantly larger than peripheral mitochondria. NMIIA KO causes perinuclear mitochondria to become even wider, a phenotype we refer to as "swollen" (1.15 ± 0.10 μm), while perinuclear mitochondria in NMIIB and NMIIC KO cells are more elongated and thinner (0.54 ± 0.06 and 0.53 ± 0.08 μm) (Figure 8, A and D). Quantification of cells with the swollen or elongated perinuclear mitochondrial phenotype shows a significant increase in cells with swollen mitochondria for NMIIA KO cells and a significant increase in cells with elongated mitochondria for NMIIC KO cells (Figure 8C). These results suggest that there are specific effects on mitochondrial diameter for the myosin II heavy chains and that these effects depend on the cellular environment of the mitochondrion.

A second morphological feature of mitochondria is their length. To assess the effect of NMII KO on mitochondrial length, we focused on peripheral cellular regions, where cells are flat and mitochondria are individually dispersed in the *Z*-plane, while they are too dense to perform such measurements in perinuclear areas. We quantified the mean mitochondrial area and mean mitochondrial number in regions of interest, following established methods (Lee *et al.*, 2016; Chakrabarti *et al.*, 2018). All three NMII KOs cause a significant increase in peripheral mitochondrial length and a decrease in mitochondrial number (Figure 9, A–C). Three myosin II inhibitors (blebbistatin, Y27632, ML7) have similar effects on mitochondrial morphology after a 1 h treatment (Supplemental Figure S6D), causing mitochondrial elongation into highly connected networks. We used a second analytical method to assess these micrographs, visually characterizing cells as having fragmented, elongated, or hyperfused mitochondria in a blinded manner. The results of this analysis are similar to those of the numerical evaluation, in that the percentage of cells possessing fragmented mitochondria decreases significantly in all three NMII KO lines (Figure 9D).

Another method to test the connectivity of the mitochondrial network is to quantify the spread of a photoactivatable mitochondrial matrix marker in a short time period (10 s), with cells possessing short mitochondria displaying less spread and those with long mitochondria displaying more extensive spread (Karbowski *et al.*, 2014). All three NMII KOs show more extensive fluorescence spread of the photoactivated marker, suggesting higher mitochondrial connectivity (Figure 9, E and F). These results suggest that KO of any NMII results in an increase in mitochondrial length. This effect is also observed upon KO or KD of INF2 (Korobova *et al.*, 2013; Chakrabarti *et al.*, 2018), suggesting a functional role for NMII in the same pathway as INF2.

Mitochondrial length can increase for two reasons: 1) a decrease in mitochondrial division or 2) an increase in mitochondrial fusion. We first examined a panel of known mitochondrial division and fusion factors for changes in abundance in NMII KO cells. Levels of the

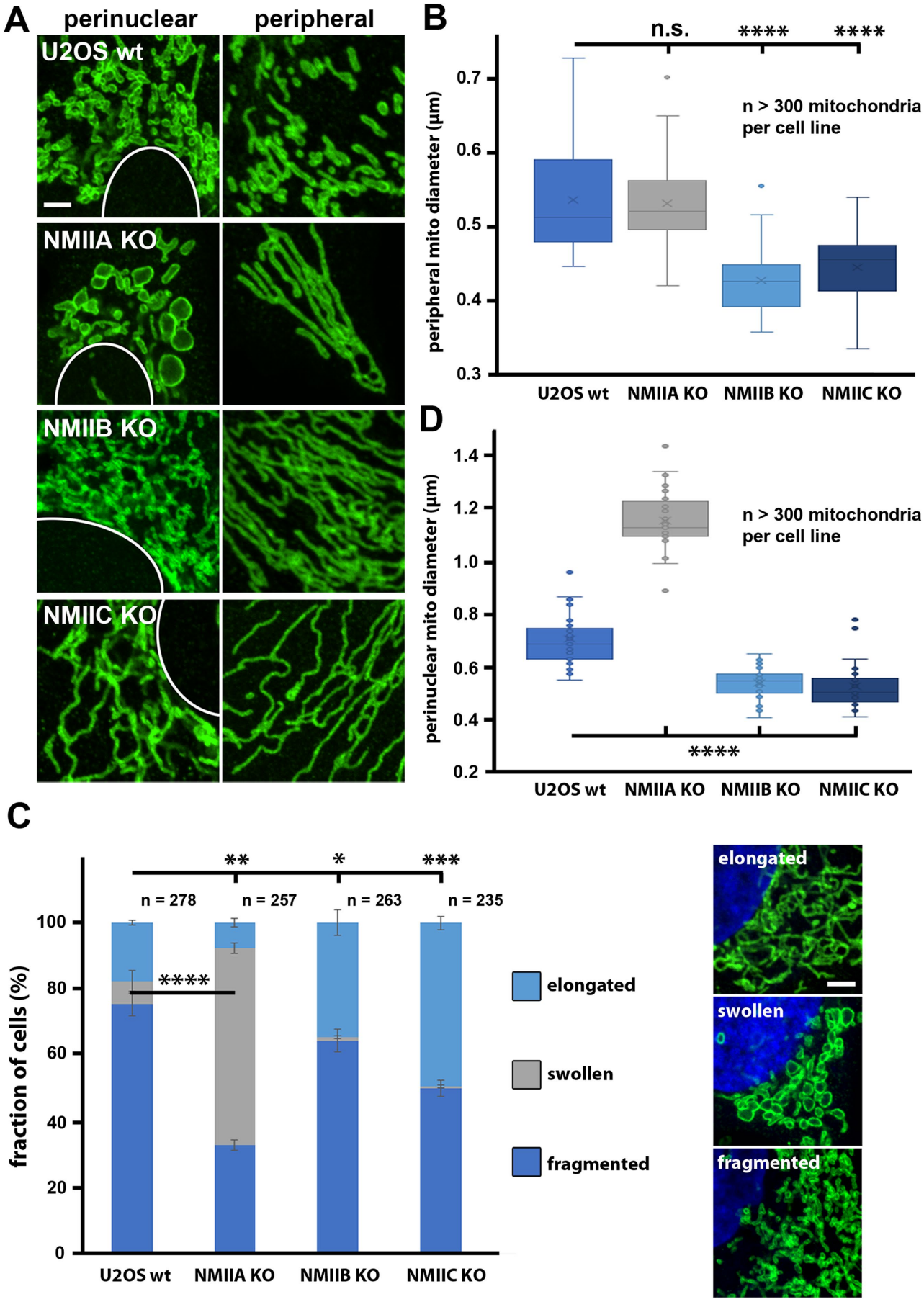
A
perinuclear
peripheral
U2OS wt
NMIIA KO
NMIIB KO
NMIIC KO
B
n.s.
****
****
peripheral mito diameter (µm)
0.7
0.6
0.5
0.4
0.3
n > 300 mitochondria per cell line
U2OS wt
NMIIA KO
NMIIB KO
NMIIC KO
D
perinuclear mito diameter (µm)
1.4
1.2
1.0
0.8
0.6
0.4
0.2
n > 300 mitochondria per cell line
****
U2OS wt
NMIIA KO
NMIIB KO
NMIIC KO
C
**
*
***
n = 278
n = 257
n = 263
n = 235
****
fraction of cells (%)
100
80
60
40
20
0
U2OS wt
NMIIA KO
NMIIB KO
NMIIC KO
elongated
swollen
fragmented
elongated
swollen
fragmented

division factors Drp1, Mff, MiD49, MiD51, and Fis1, as well as the main fusion factors Mfn1, Mfn2, and OPA1, are similar to WT for all KOs (Figure 9G). One important step in mitochondrial division is recruitment of the dynamin GTPase Drp1 to mitochondria, with Drp1 mediating OMM constriction (Kraus *et al.*, 2021). Drp1 accumulates as "puncta" on mitochondria, indicative of oligomerization, and this accumulation is dependent on INF2 (Korobova *et al.*, 2013; Ji *et al.*, 2015). We used a GFP-Drp1 knock-in cell line (Ji *et al.*, 2017) to assess the effects of KD of NMIIA, B, and C on Drp1 recruitment to mitochondria. All three NMII KDs significantly decrease the colocalization of GFP-Drp1 puncta with mitochondria (Figure 10), indicative of decreased Drp1 recruitment. This reduction in Drp1 recruitment is similar to that caused by INF2 KD. Taken together, the results suggest that mitochondrial elongation and hyperconnectivity upon loss of NMII heavy chains is a result of hampered mitochondrial fission.

DISCUSSION

In this work, we make a number of surprising findings concerning NMII, mostly focused on CIA but with impact for all NMII cellular functions. First, NMII is activated and recruited rapidly (within 1 min) to the CIA network. Second, all three NMII heavy chains appear to be involved in the organization and function of the CIA network in U2OS cells. A third finding is that the suppression of NMIIA heavy chain, by either KO or KD, causes a large drop in the amount of MRLC. We frame this discussion around these findings.

A caveat of our results is that only one clone for each KO was tested. In terms of potential off-target effects, the levels of 14 other proteins appear unaffected in the NMIIA, B, and C KO lines (Figure 9G). These proteins include actin, tubulin, INF2, and proteins involved in mitochondrial division and fusion. One protein whose level is affected is MRLC, which is depleted in both NMIIA KO and KD. It is unclear whether this MRLC reduction has an effect on NMIIB or NMIIC function, or on their bound MRLC. Given that 17% MRLC signal remains upon NMIIA KO (Figure 2, E and F) and that NMIIB and NMIIC are present at only 6 and 0.4% of NMIIA, respectively (Figure 2, A and B), it is possible that the loss of MRLC represents only that directly bound to NMIIA.

NMII activation (as assessed by MRLC phosphorylation) reaches a maximum within 1 min of ionomycin or histamine stimulation (Figure 1, B and E), and NMII is recruited to the CIA network on the same timescale (Figures 1D and 6 and Supplemental Figure S5). This recruitment seems to be specific for NMII, as another actin-binding protein, tropomyosin 3, is not enriched in this actin structure. The fact that ionomycin causes a specific increase of NMII in the actin-rich cell pellet (Figure 5D) suggests that CIA-bound NMII represents newly activated molecules rather than redistribution from other NMII-rich structures, such as stress fibers. The rapidity of NMII activation/recruitment is impressive, considering that the fundamental NMII molecular unit (which we call the "dimer," consisting of the dimeric heavy chain attached to one essential light chain and one MRLC per heavy chain) presumably must oligomerize into a minifilament of 14–30 dimers during this time.

NMII filaments are highly dynamic in lamellae of migrating cells (Vicente-Manzanares *et al.*, 2007; Fenix *et al.*, 2016; Beach *et al.*, 2017; Hu *et al.*, 2017; Shutova *et al.*, 2017), denoting the ability to assemble rapidly. In these previous studies, however, it was difficult to determine whether the newly assembled NMII filaments had been recently activated or were the result of recycled NMII dimers that had been phosphorylated previously. It is also possible that the functional NMII unit in CIA is not a filament but a smaller structure, possibly even an activated dimer. Active NMII dimers are embedded in nodal sites in the cytokinetic ring of fission yeast (Laporte *et al.*, 2011; Laplante *et al.*, 2016; McDonald *et al.*, 2017). There is also evidence that active NMII dimers exist in the cytosol in mammal culture cells (Shutova *et al.*, 2014).

Another intriguing feature is that the MRLC remains phosphorylated for an extended time, while the CIA actin network disassembles within 3 min (Figure 1, B–E). The fate of the activated NMII after release from the CIA network is unclear. One possibility is that the active NMII is incorporated into other dynamic NMII-containing structures such as ventral stress fibers, transverse arcs, or cortical actin.

It is unclear at present as to whether NMII functions in CIA actin network assembly or in organization of the CIA network. Depletion of any single NMII decreases the apparent density of the network, as observed by an imaging assay monitoring TRITC-phalloidin (Figure 4, A and B), suggesting a decrease in overall polymerized actin. Similarly, our live-cell imaging assay also shows a decrease of the F-tractin intensity increase induced by CIA. However, our biochemical extraction assay shows that the amount of actin pelleted by ultracentrifugation is not altered significantly by KO of any single NMII (Figure 5), which could suggest that the decreased network staining is due to a change in organization such as decreased bundling of the network. There are caveats to all of these assays, so additional methods are needed to resolve this issue. What is clear is that the morphology of the CIA network depends on NMII, and it remains to be determined whether NMII plays a role in actin assembly, actin network organization, or both.

It is unclear whether NMII also serves a contractile function in CIA. The fact that CIA stimulates ER-to-mitochondrial calcium exchange through increasing ER-mitochondrial contact (Chakrabarti *et al.*, 2018) could suggest that NMII-based contraction of the CIA network drives this rapprochement of the two organelles.

An interesting result is that all three NMII heavy chains appear to take part in the CIA network. KO of any single NMII decreases both the density of the network (Figure 4, A and B) and its downstream

FIGURE 8: Perinuclear and peripheral mitochondria differ in their response to NMII KO. (A) Fixed-cell images of WT or NMII KO U2OS cells stained for mitochondria (Tom20), focusing on two subcellular regions: perinuclear (left) and peripheral (right). White outlines indicate the location of the nucleus for perinuclear examples. Bar is 3 μm. (B) Quantification of diameters of peripheral mitochondria from images similar to those in panel A. Unpaired *t* test with *p* values as follows: 0.78 (n.s.) for NMIIA KO and <0.0001 (****) for NMIIB/C KOs. At least 300 mitochondria (from more than 30 individual cells and three experimental replicates) per cell line were measured. (C) Classification of cells in terms of perinuclear mitochondrial morphology, binning cells into "elongated," "swollen," or "fragmented." Representative examples of each category at right (blue is 4,6-diamidino-2-phenylindole). Bar is 3 μm. Unpaired *t* test with *p* values for category "elongated mitochondria" as follows: 0.0026 (**) for NMIIA KO, 0.0123 (*) for NMIIB KO, and 0.0001 (***) for NMIIC KO. Comparison of WT and NMIIA KO cells for "swollen mitochondria" with *p* value < 0.0001 (****). Error bars are SEM. (D) Quantification of diameters of perinuclear mitochondria from images similar to those in panel A. Unpaired *t* test with *p* values < 0.0001 (****) for all NMII KOs. At least 300 mitochondria (from more than 30 individual cells and three experimental replicates) per cell line were analyzed.

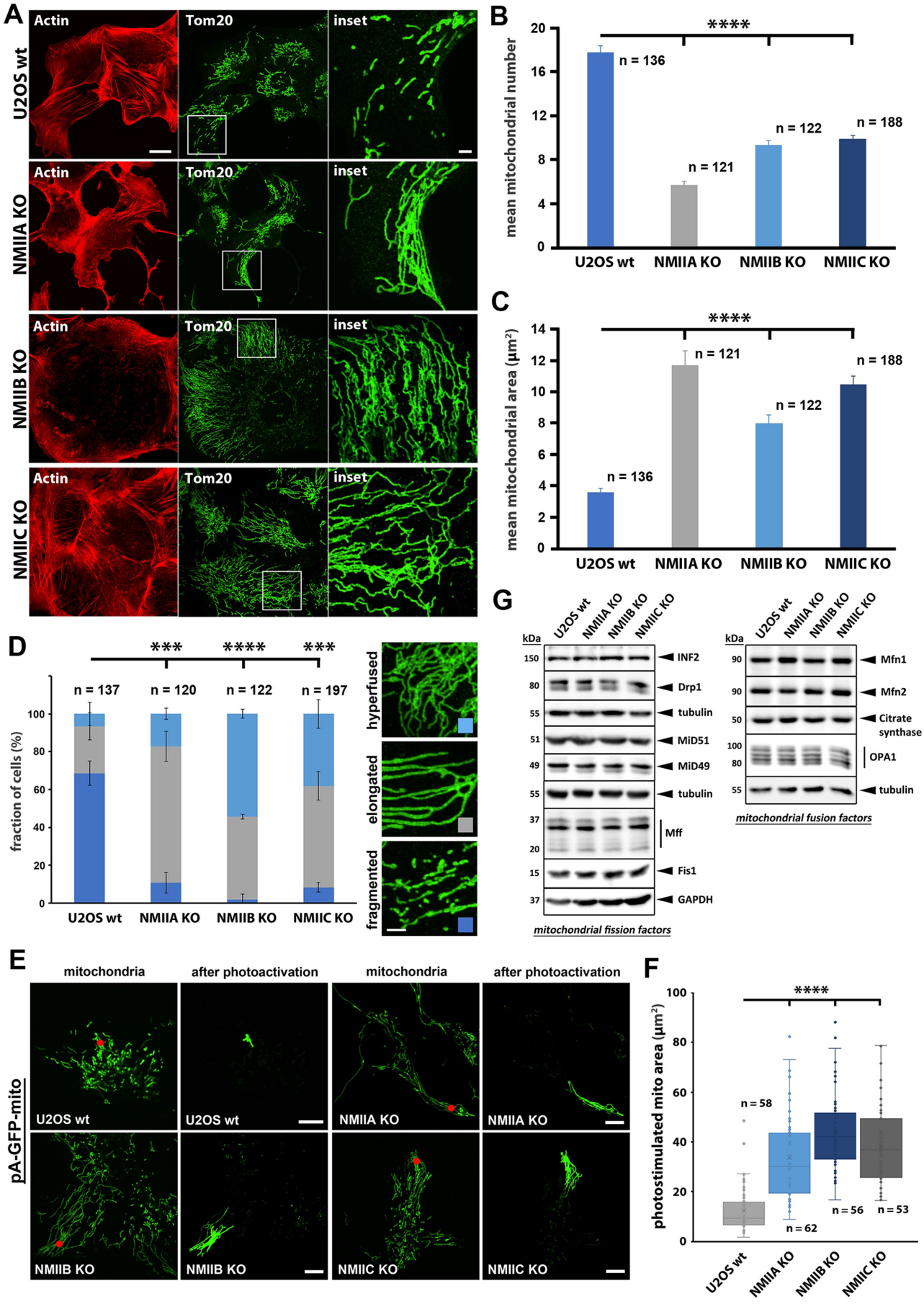
A
Actin
Tom20
inset
U2OS wt
NMIIA KO
NMIIB KO
NMIIC KO
B
mean mitochondrial number
****
n = 136
n = 121
n = 122
n = 188
U2OS wt
NMIIA KO
NMIIB KO
NMIIC KO
C
mean mitochondrial area (µm²)
****
n = 136
n = 121
n = 122
n = 188
U2OS wt
NMIIA KO
NMIIB KO
NMIIC KO
D
fraction of cells (%)
***
****
***
n = 137
n = 120
n = 122
n = 197
U2OS wt
NMIIA KO
NMIIB KO
NMIIC KO
hyperfused
elongated
fragmented
G
kDa
U2OS wt
NMIIA KO
NMIIB KO
NMIIC KO
INF2
Drp1
tubulin
MiD51
MiD49
tubulin
Mff
Fis1
GAPDH
mitochondrial fission factors
Mfn1
Mfn2
Citrate synthase
OPA1
tubulin
mitochondrial fusion factors
E
mitochondria
after photoactivation
mitochondria
after photoactivation
pA-GFP-mito
U2OS wt
U2OS wt
NMIIA KO
NMIIA KO
NMIIB KO
NMIIB KO
NMIIC KO
NMIIC KO
F
photostimulated mito area (µm²)
****
n = 58
n = 62
n = 56
n = 53
U2OS wt
NMIIA KO
NMIIB KO
NMIIC KO

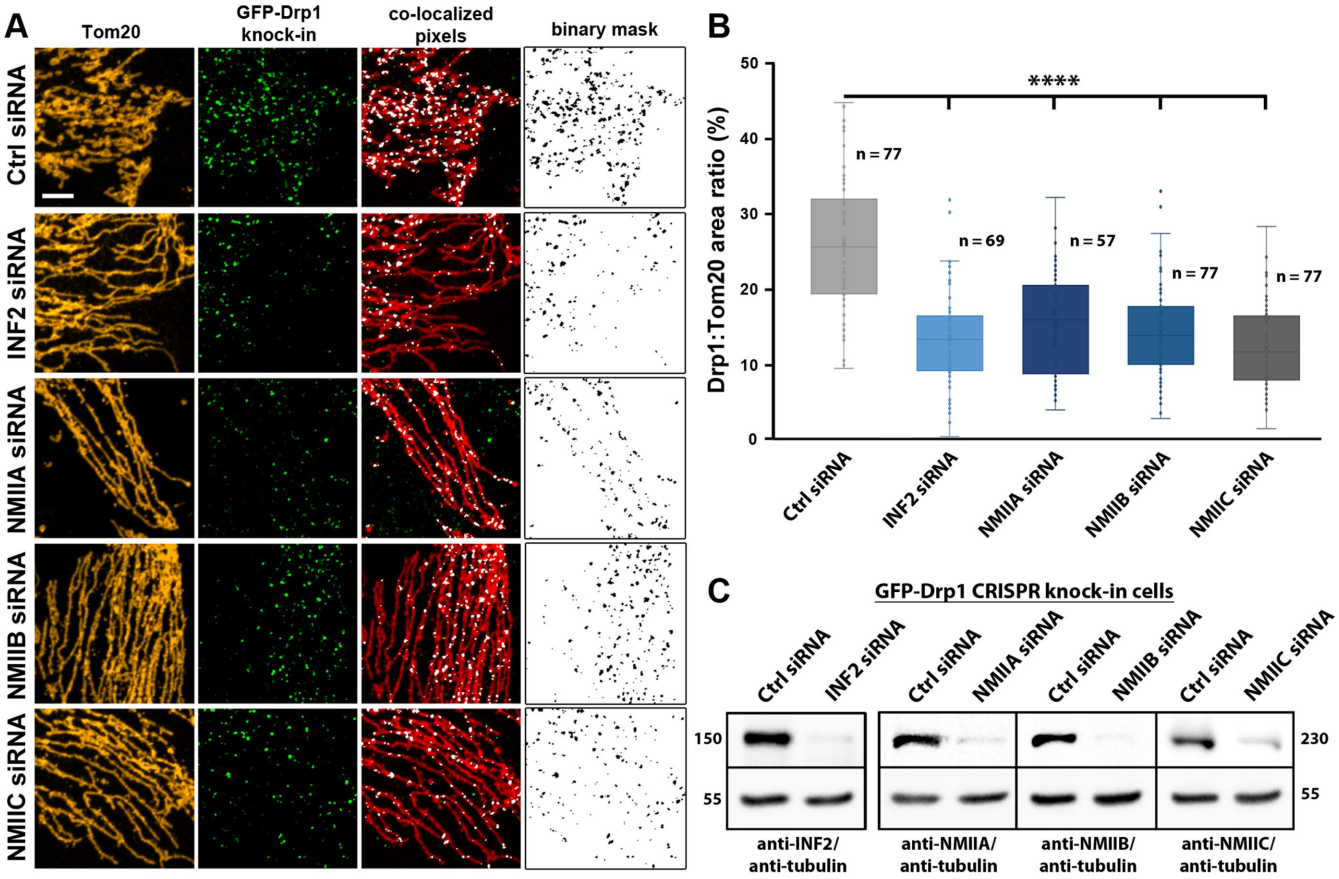

FIGURE 10: NMII proteins are required for optimal mitochondrial division. (A) Fixed-cell imaging of GFP-Drp1 knock-in U2OS cells transfected with control siRNA or siRNA against INF2, NMIIA, NMIIB, or NMIIC. Mitochondria stained with anti-Tom20. Right-hand panel shows a binary mask of the GFP-Drp1 pixels that overlay with the mitochondrial signal. GFP-Drp1 signal has been thresholded to exclude the uniform cytoplasmic signal, to focus on the oligomeric puncta. Bar is 5 μm. (B) Plot of mitochondrially associated Drp1 puncta in each of the cell types. Unpaired *t* test with *p* values < 0.0001 (****). (C) Western blots showing effectiveness of siRNAs toward their targets in GFP-Drp1 knock-in cells.

effects on mitochondria (Figures 7–10), although some mitochondrial effects seem to be specific for the loss of NMIIA. It is possible that the effect of NMIIA KO is indirect, because this KO also results in a dramatic loss of MRLC protein (Figure 2, E and F, and Supplemental Figure S2A). The relative affinities of the three major MRLCs in nonmuscle cells (Myl9, Myl12A, and Myl12b) for NMIIA, NMIIB, and NMIIC are unknown, but they are suspected to be able to bind to all (Heissler and Sellers, 2015), and the specific MRLC bound to each NMII heavy chain has not been determined. Also not known is the effect of distinct MRLCs on NMII regulation and function. In addition, one or more of these MRLCs can interact with other myosin classes, such as myosin 15 (Bird *et al.*, 2014) and myosin 19 (Lu *et al.*, 2014). However, the fact that NMIIA is rapidly enriched in the CIA network suggests its active participation.

One question concerning the functions of specific NMII heavy chains is whether they are all part of the same filament. NMIIA and NMIIB can coassemble into filaments in lamellae (Beach *et al.*, 2014; Shutova *et al.*, 2014, 2017). However, their dynamics in these

FIGURE 9: Loss of NMII proteins causes mitochondrial elongation and hyperconnectivity. (A) Fixed-cell imaging of WT or NMII KO U2OS cells stained for actin filaments (TRITC-phalloidin) and mitochondria (Tom20). Bar is 20 μm in overview images and 3 μm in magnifications. (B) Mitochondrial number measurements from ROIs similar to those shown in panel A. Unpaired *t* test with *p* values <0.0001 (****). Error bars are SEM. (C) Mitochondrial area measurements from ROIs similar to those shown in panel A. Unpaired *t* test with *p* values < 0.0001 (****). Error bars are SEM. (D) Plot representing the fraction of cells harboring a certain mitochondrial phenotype, characterized as fragmented, elongated, or hyperfused. A representative example for each category is given on the right. Bar is 3 μm. Unpaired *t* test for "fragmented mitochondria" populations with *p* values as follows: 0.0003 (***) for NMIIA KO, <0.0001 (****) for NMIIB KO, and 0.0001 (***) for NMIIC KO. Error bars are SEM. (E) Live-cell images of WT or NMII KO U2OS cells expressing a photoactivatable GFP construct localized to the mitochondrial matrix. For each cell type, the left image shows the entire mitochondrial network (enhanced contrast) as well as the activation area (red dot), while the right image shows the area of the photoactivated GFP spread 10 s after activation. Bars are 10 μm. (F) Quantification of the area of photoactivated signal after 10 s, from movies similar to those shown in panel E. Unpaired *t* test with *p* values < 0.0001 (****). (G) Western blots probing the expression levels of typical mitochondrial division and fusion factors in U2OS WT and NMII KO cells as indicated.

filaments and in the lamellum are different, with NMIIA turning over more rapidly (Vicente-Manzanares *et al.*, 2007; Shutova *et al.*, 2017). NMIIC can copolymerize with NMIIA/NMIIB (Beach *et al.*, 2014), but it is unclear what the size of the resulting filaments might be, because NMIIC alone assembles into filaments of 14 dimers, whereas NMIIA and NMIIB filaments are close to 30 dimers (Billington *et al.*, 2013). NMIIA and NMIIC colocalize throughout the entire cell body in U2OS cells (Beach *et al.* 2014), suggesting that NMIIC could fine-tune the organization and turnover of higher-ordered NMIIA filament stacks.

Functionally, there is evidence both for independent NMII functions and for shared functions in other cellular processes. NMIIA and NMIIB are present in a graded manner in the lamellum of migrating cells, with NMIIA more enriched toward the front and NMIIB more enriched toward the back (Vicente-Manzanares *et al.*, 2008; Beach *et al.*, 2014; Shutova *et al.*, 2017). Coupled with differences in their specific motor properties, this graded distribution results in differential contractile properties in different cellular regions. In the actin cortex, NMIIA appears to be the sole NMII heavy chain needed for bleb retraction (Taneja and Burnette, 2019), whereas maintenance of cortical tension in mitotic/cytokinetic cells requires both NMIIA and NMIIB, but for distinct purposes (Taneja *et al.*, 2020). The requirements for specific NMII heavy chains in cytokinesis are unclear, with overexpression of any single NMII being able to rescue cytokinesis in KO cells with cytokinetic defects (Ma and Adelstein, 2014).

In particular, the role of NMIIC is poorly understood for any cellular process. NMIIC KO mice have been reported to have no systemic defects (Ma *et al.*, 2010; Fu *et al.*, 2016), and the only consistently reported defect is to hearing (Fu *et al.*, 2016; Kim *et al.*, 2017). In accordance with that observation, NMIIC has been shown to determine the length of growing microvilli by regulating actin turnover (Chinowsky *et al.*, 2020). More recently, a mutation in the NMIIC tail was associated with peripheral neuropathy, with evidence that one cellular defect is in mitochondrial division (Almutawa *et al.*, 2019). The latter work fits well with our findings, showing that NMIIC has a disproportionate role in CIA and its downstream consequences, including mitochondrial division, in U2OS cells (Figures 7–10). We use the term "disproportionate" because NMIIC is by far the least abundant NMII heavy chain in U2OS cells, but its deletion has as much of an effect as the other NMIIs. By quantitative Western blotting, we find the molar ratios of NMIIA:NMIIB and NMIIC to be 220:14:1 in U2OS cells (Figure 2, A and B), with a proteomic approach providing ratios in the same order of magnitude (Supplemental Figure S1G).

In a recent publication comparing NMII KO U2OS cells, NMIIA appears to be the force initiator for overall cellular tension, while NMIIB stabilizes tension on longer timescales. Interestingly, this publication found that, in NMIIC KO cells, contraction forces did not relax back, indicating that NMIIC might control force maintenance and relaxation, especially in a dynamical context (Weißenbruch *et al.*, 2021). Likewise in CIA, NMIIC appears to be part of the myosin II contractome, possibly serving as the regulator of filament assembly or dynamics.

Our findings on NMII effects on mitochondria raise at least two interesting issues on control of mitochondrial morphology. First, all NMII proteins are required for maximal stimulus-induced mitochondrial calcium increase, similar to our past results on CIA (Chakrabarti, 2018). Second, we find a clear difference in mitochondrial diameter between peripheral and perinuclear mitochondria in WT U2OS cells, with the perinuclear mitochondria having larger diameters. Morphological differences between these two populations have been observed previously (Collins, 2002) but have not received much attention. The fact that KOs of specific NMII proteins have specific (and opposite in some cases) effects on mitochondrial diameter suggests specific morphological control of these populations. The techniques utilized here are not adequate to assess NMII KO effects on perinuclear mitochondrial length due to the difficulty in deconvolving the perinuclear mitochondria in three-dimensional (3D) space to obtain traces of entire mitochondria. Ultimately, more extensive 3D microscopy will be required.

CIA participates in two facets of mitochondrial fission: "preconstriction" of mitochondria, driven by mitochondrial calcium uptake and inner mitochondrial membrane dynamics (Cho *et al.*, 2017; Chakrabarti *et al.*, 2018); and recruitment of Drp1 for constriction of the OMM (Korobova *et al.*, 2013; Ji *et al.*, 2015). NMII clearly plays a role in both processes (Korobova *et al.*, 2014; Chakrabarti *et al.*, 2018), and here we show that all three NMII heavy chains participate. Recent ultrastructural studies show that INF2-generated actin filaments often enrich at mitochondrial constriction sites, but at a variety of angles (Yang and Svitkina, 2019). Furthermore, both NMIIA and NMIIB enrich near to, but not at these constriction sites (Yang and Svitkina, 2019). These findings might be complicated by the existence of both INF2-CAAX and INF2-nonCAAX in the cells used, which creates two distinct CIA networks: one attached to the ER and one not (Ramabhadran *et al.*, 2011). The elucidation of NMII roles in force production during this process requires detailed correlative ultrastructural studies using cell lines with CIA triggered by INF2-CAAX or INF2-nonCAAX individually.

MATERIALS AND METHODS

Request a protocol through *Bio-protocol*.

Plasmids and siRNA oligonucleotides

The GFP-F-tractin plasmid (Johnson and Schell, 2009) was a gift from A. Pasapera (NIH, Bethesda, MD). The mito-R-GECO (K_d = 0.48 μM for calcium) construct was a gift from Y. M. Usachev (University of Iowa, IA) and has been described previously (Wu *et al.*, 2014). GFP-ER-GCaMP6-150 (K_d = 150 μM for calcium) was described previously (de Juan-Sanz *et al.*, 2017) and is available from Addgene (86918). Flag-tagged Myl6 (ELC), -Myl9, and -Myl12A (MRLCs) constructs were kindly provided by M. Vincente-Manzanares (University de Salamanca, Salamanca, Spain). Human, full-length GFP-tagged NMIIA and NMIIB were gifts from R. Horwitz and B. Adelstein (NIH, Bethesda, MD). Human, full-length NMIIC-GFP was kindly provided by T. Shutt (University of Calgary, Alberta, Canada) and described in Almutawa *et al.* (2019). Mito-PAGFP was obtained from R. Youle (NIH, Bethesda, MD) and published in Karbowski *et al.* (2014).

The following oligonucleotides for all siRNA used were synthesized by Integrated DNA Technologies:

INF2 (aa 829-837): 5′-GAGCGGAUGAUCUCCAGGUUGAUCCCU-3′; NMIIA (exon 38): 5′-GCCACGCCCAGAAGAACGAGAAUGC-3′; NMIIB (CDS/12): 5′-UCAAUAAAGCUCUGGAUAGGACCAA-3′ and NMIIC (CDS/39): 5′-CGCCACAAGAUGACCAUUGCUGCCC-3′. Silencer negative control (IDT) was 5′-CGUUAAUCGCGUAUAAUACGCGUAU-3′.

Cell culture

Human osteosarcoma U2OS cells, purchased from the American Type Culture Collection (ATCC; HTB96), were grown in DMEM (Corning; 10-013-CV) supplemented with 10% newborn calf serum (Hyclone; SH30118.03). Human cervical cancer HeLa cells were procured from ATCC (CCL-2) and grown in DMEM (Corning; 10-013-CV) supplemented with 10% fetal bovine serum (F4135; Sigma). INF2 KO U2OS cells were generated in our laboratory using CRISPR/Cas9 and were reported previously (Chakrabarti *et al.*, 2018). The GFP-Drp1 knock-in U2OS cell line made by CRISPR/Cas9 was

described elsewhere (Ji *et al.*, 2017). The cell line expresses GFP-Drp1 at 50% of the total Drp1 level, with the remaining Drp1 being unmodified (overall Drp1 level unchanged from control cells). All cell lines were cultivated at 37°C with 5% CO_2.

Transfections

For plasmid transfections, cells were seeded at 5×10^5 cells per 35 mm well ~16 h before transfection. Transfections were performed in OPTI-MEM medium (Life Technologies; 31985062) with 2 µl of Lipofectamine 2000 (Invitrogen; 11668) per well for 6 h, followed by trypsinization and replating onto glass-bottomed dishes (MatTek Corporation; P35G-1.5-14-C) at ~3.5×10^5 cells per well. Cells were imaged in live-cell medium (DMEM with 25 mM D-glucose, 4 mM -glutamine, and 25 mM HEPES, supplemented with 10% newborn calf serum) ~24 h posttransfection. For all experiments, the following amounts of DNA were transfected per well (individually or combined for cotransfections): 800 ng for mito-R-GECO, 200 ng for GFP-F-tractin, 300 ng for ER-GCaMP6-150, 100 ng for mito-PAGFP, and 500 ng for GFP-tagged NMII constructs.

For siRNA transfections, 1×10^5 cells were plated on six-well plates, and 2 µl RNAi max (Invitrogen; 13778) and 63 pg siRNA were used per well. siRNA transfections were repeated after 48 h, and cells were analyzed 96 h posttransfection. KD efficiency was routinely tested on cell extracts by Western blotting.

CRISPR/Cas9-mediated generation of NMII KO cell lines

U2OS cells were genome-edited for deletion of individual NMII genes *MYH9* (NMIIA), *MYH10* (NMIIB), and *MYH14* (NMIIC) using the CRISPR/Cas9 technology. CRISPR guideRNAs (gRNAs) were as follows: 5′-TGGGTGCCTTCCGACAAGAG-3′ for NMIIA, 5′-CTGAAGGATCGCTACTATTC-3′ for NMIIB, and 5′-GACGGCCCGGCGTCTCGTGT-3′ for NMIIC, respectively. All genes were disrupted targeting a specific genomic region in respective exon 1. Selected gRNAs were cloned into pSpCas9(BB)-2A-Puro (Addgene: 48139) and sequence-verified using oligo 5′-GCACCGACTCGGTGCCAC-3′, and 1 µg of the plasmid was transfected overnight using Lipofectamine 2000 as described above. The next day, transfected cells were replated into medium containing 2.5 µg/ml puromycin and selected for 2 d. Afterward, remaining cells were allowed to regrow for a few days in regular growth medium before being diluted to ~0.5 cells per well of a 96 well plate to obtain single cell–derived clones. Single-cell clones were expanded and screened for the absence of respective NMII protein expression by Western blotting using highly specific antibodies (Supplemental Figure S1C).

Ionomycin/histamine treatments

For ionomycin/histamine treatments, 5×10^5 cells were seeded in 35 mm dishes. The following day, regular growth medium was replaced by 1 ml of live-cell medium (DMEM with 25 mM D-glucose, 4 mM D-glutamine, and 25 mM HEPES, supplemented with 10% newborn calf serum). Another 1 ml of live-cell medium containing 8 µM ionomycin (I0634; Sigma; from a 1 mM stock in DMSO) was added swiftly in a circular motion onto the plate, making the final ionomycin concentration 4 µM. The same procedure was applied for histamine treatments, with a final concentration of 100 µM (H7125; Sigma; from a 100 mM stock in DMSO). Stimulations were carried out for the indicated time durations (Figure 1, B and E), followed by instant medium removal and cell lysis for Western blotting.

Myosin II inhibitor treatments

Cells on MatTek dishes for live-cell imaging (Supplemental Figure S6A) or cells on fibronectin-coated coverslips for immunolabeling (Supplemental Figures S3A and S6D) were treated with either 50 µM blebbistatin (B0560; Sigma; from a 20 mM stock in DMSO), 20 µM Y27632 (688000; Calbiochem; from a 5 mM stock in DMSO), or 30 µM ML7 (475880; Sigma; from a 50 mM stock in DMSO) in regular growth medium for 1 h before the experiment. For live-cell imaging, the respective inhibitor was kept in the imaging medium.

Western blotting and antibodies

For preparation of whole-cell extracts, confluent cell layers in 35 mm dishes were washed 3× with phosphate-buffered saline (PBS), lysed using ~300 µl of 1×DB (50 mM Tris-HCl, pH 6.8, 2 mM EDTA, 20% glycerol, 0.8% SDS, 0.02% bromophenol blue, 1000 mM NaCl, 4 M urea), and boiled for 5 min at 95°C, and genomic DNA was sheared using a 27×G needle. Proteins were separated by standard SDS–PAGE and transferred to a PVDF (polyvinylidine difluoride) membrane (Millipore). The membrane was blocked with TBS-T (20 mM Tris-HCl, pH 7.6, 136 mM NaCl, and 0.1% Tween-20) containing 3% bovine serum albumin for 1 h and then incubated with the primary antibody solution at 4°C overnight. After being washed with TBS-T, the membrane was incubated with horseradish peroxidase (HRP)-conjugated secondary antibodies (goat anti mouse #1721011; Bio-Rad or goat anti rabbit #1706515; BioRad) for 1 h at room temperature. Chemiluminescence signals were detected upon incubation with ECL Prime Western Blotting Detection Reagent (45-002-40; Cytiva Amersham) and recorded with an ECL Chemocam imager (SYNGENE G:BOX Chemi XRQ). For LI-COR Western blots, membranes were incubated with either IRDye 680 goat anti-mouse (926-68070; LI-COR), IRDye 800CW goat anti-rabbit (926-32211; LI-COR), or IRDye 680 donkey anti-chicken (926-68075) secondary antibodies for 1 h at room temperature. Signals were detected using the LI-COR Odyssey CLx imaging system.

Primary antibodies used were as follows: NMIIA (rabbit; 3403; Cell Signaling Technology; 1:1000). NMIIB (rabbit; 3404; Cell Signaling Technology; 1:1000). NMIIC (rabbit; 8189; Cell Signaling Technology; 1:1000). MRLC (rabbit; 3672; Cell Signaling Technology; 1:1000). Phospho (S19)-MRLC (rabbit; 3671; Cell Signaling Technology; 1:1000). pan-NMII (rabbit; BTI-561; Biomedical Technologies; 1:400). GAPDH (G-9, mouse; Santa Cruz Biotechnology; 1:500). Tubulin (DM1-α, mouse; T9026; Sigma; 1:10,000). Actin (mouse; mab1501R; Millipore; 1:1000). Self-made rabbit polyclonal anti-INF2 antibody was described previously (Ramabhadran *et al.*, 2011; against amino acids 941–1249 of human INF2-CAAX; 1:1000). An additional self-made chicken polyclonal anti-INF2 antibody against the same amino acids of INF2 was used in the myosin II quantification experiments. FLAG-HRP coupled (mouse; A8592; Sigma; 1:1000). Arp2 (rabbit; ab129018; Abcam; 1:500). Arp3 (mouse; A5979; Sigma; 1:500). α-Actinin (mouse; 05-384; Upstate; 1:500). Drp1 (mouse; 611112; BD Transduction Laboratories; 1:1000). Mff (rabbit; 17090-1-AP; Proteintech; 1:1000). Fis1 (rabbit; 10956-1-AP; Proteintech; 1:1000). MiD51 (rabbit; 20164-1-AP; Proteintech; 1:500). MiD49 (rabbit; 16413-1-AP; Proteintech; 1:500). OPA1 (mouse; 612606; BD Biosciences; 1:2000). Mfn1 (rabbit; 14739; Cell Signaling Technology; 1:1000). Mfn2 (rabbit; 11925; Cell Signaling Technology; 1:1000), and citrate synthase (rabbit; 16131-1-AP; Proteintech; 1:1000).

Note that anti-MRLC antibody is listed as being directed against the N-terminal amino acids of human myosin light chain 2, which, by the company-supplied UniProt ID number (P24844) and Entrez-Gen ID number (10398), corresponds to the Myl9 gene. Of the 20 N-terminal amino acids of Myl9, 17 are identical to those of Myl12A and 19 are identical to those of Myl12B, the two other predominant

MRLCs expressed in U2OS cells according to the Human Protein Atlas. We show in Supplemental Figure S2B that the antibody indeed cross-reacts with Myl12A.

Western blot intensity measurements

To quantify relative protein levels (Figures 1, B and C, 2, C–F, and 5, A–C), intensity measurements on exposed Western blot membranes were performed using ImageJ ("measure" plug-in). Protein bands of interest were outlined, and mean signal intensities were measured. Regions of the same size were measured in background areas and subtracted from corresponding protein bands. Protein band intensities were then normalized to those of corresponding loading controls (such as GAPDH, tubulin, or actin). Corresponding data were plotted as bar charts using Microsoft Excel.

Quantification of NMII and actin concentrations by quantitative Western blotting

Quantitative Western blotting was used to determine endogenous NMII and actin concentrations in U2OS cells (Figure 2, A and B, and Supplemental Figure S1). To prepare cell extracts, U2OS cells were trypsinized, washed, and resuspended in PBS, quantified for cell number (TC20; BioRad) and protein concentration (Bradford), and then extracted with 4% SDS/10 mM dithiothreitol (DTT) followed by cysteine capping with 30 mM freshly made N-ethylmaleimide (Sigma-Aldrich). Cellular protein was calculated at 0.37 ± 0.045 ng/cell. A linear range of cell extract for signal for each protein by Western blot was determined and was found to be 0.5–3 µg for NMIIA, 1–5 µg for NMIIB, 2–10 µg for NMIIC, and 0.1–2 µg for actin. For the concentration determination by quantitative Western blot, fixed amounts of cell extract were used (1.5, 2, 3, and 0.3 µg for NMIIA, NMIIB, NMIIC, and actin, respectively) along with various amounts of purified NMII proteins (kind gifts from James Sellers, National Institutes of Health) as internal standards. Proteins were resolved by SDS–PGE (5 and 7.5% for NMII and actin, respectively) and detected by Western blot using an Odyssey CLx imager (LI-COR). Primary antibodies were incubated as the rabbit anti-NMII antibody of choice (1:500) and the chicken anti-INF2 antibody (1 µg/ml) overnight at 4°C. Secondary antibodies were incubated as the respective LI-COR anti-rabbit and anti-chicken antibodies (1:5000 each) overnight at 4°C. Band intensities were quantified with ImageStudioLite (LI-COR), using the median band intensity and subtracting background of the same area directly below the band of interest. Cytosolic concentrations were estimated using a cytoplasmic volume (3.14 pl/cell) calculated for COS-7 cells by subtracting volumes of nucleus (0.902 pl), endoplasmic reticulum (1.538 pl), peroxisome (0.186 pl), mitochondria (0.179 pl), lysosome (0.089 pl), and Golgi (0.042 pl) from total cell volume (6.074 pl) obtained from Valm *et al.* (2017).

NMII ratio quantification by mass spectrometry

U2OS cells were grown to 100% confluency in six-well plates, trypsinized, and washed 3× with PBS. Cell pellet was extracted with 1% SDS, 50 mM Tris, pH 8.7, 150 mM NaCl, 5 mM DTT and boiled. Cysteines were capped with 15 mM iodoacetamide (A3221; Sigma). Six wells were extracted individually, and total protein amounts were balanced by preliminary Coomassie staining of SDS–PAGE gels. Samples were separated by SDS–PAGE (7.5% acrylamide) and stained with Coomassie, and a band approximately 5 mm centered on the 250 kDa standard (BioRad Precision Plus dual color) was excised, destained, and digested with Lys-C (Wako Chemicals USA) in 50 mM ammonium bicarbonate overnight at 37°C. Peptides were extracted using 5% formic acid/50% acetonitrile (ACN) and dried. Peptides were analyzed on a Q Exactive Plus mass spectrometer (ThermoScientific) equipped with an Easy-nLC 1000 (ThermoScientific). Raw data were searched using COMET in high resolution mode (Eng *et al.*, 2013), Lys-C enzyme specificity with up to three missed cleavages, and carbamidomethylcysteine as fixed modification. Oxidized methionine was searched as variable modifications. Quantification of LC-MS/MS spectra was performed using MassChroQ (Valot *et al.*, 2011). Protein amounts were corrected based on total protein amount. Areas associated with unique matching peptides were summed.

Actin pelleting assay

U2OS WT, INF2 KO, or NMII KO cells were seeded 1×10^6 cells per 35 mm well the day before the experiment. For LatA samples, cells were pretreated with 2 µM LatA (428021; Calbiochem) in live-cell medium for 20 min followed by ionomycin stimulation. U2OS WT, NMII KO, or INF2 KO cells were treated with either a final concentration of 4 µM ionomycin or an equal volume of DMSO in live-cell medium for 45 s. Medium was removed quickly, and cells were extracted with 400 µl of extraction buffer (1×Na50MEH [500 mM NaCl, 20 mM $MgCl_2$, 5 mM EGTA (ethylene glycol-bis-(2-aminoethylether)-*N*,*N*,*N*,*N*-tetraacetic acid), 100 mM HEPES], 1 mM DTT, 2 µM phalloidin, 2 µM LatA, and 1% Triton X-100). Samples (150 µl) of each cell lysate were taken as input and mixed with 50 µl 4× sample buffer (500 mM Tris, pH 6.8, 4 mM EDTA, 40% glycerol, 8% SDS). Cell lysate (200 µl) was transferred to a TLA100 tube, and samples were centrifuged at 80,000 rpm in a TLA100 rotor for 22 min at 4°C. Afterward, 150 µl of the supernatant containing monomeric actin was collected and mixed with 50 µl 4× sample buffer. The pellet, containing the filamentous actin fraction, was carefully washed with 200 µl of 1×Na50MEH with 1% Triton X-100 before it was resuspended in 267 µl of 1× sample buffer. All samples were boiled at 95°C for 5 min. Ten microliters of each sample was loaded onto SDS gels, standard Western blotting was performed, and anti-actin (mouse; mab1501R; Millipore; 1:1000) antibody was used to detect the amount of actin in each fraction and condition (Figure 5).

Immunofluorescence staining

For immunolabeling of proteins of interest, cells were seeded subconfluently on fibronectin (F1141; Sigma)-coated (1:100 in PBS) coverslips (72222-01; Electron Microscopy Sciences) in 35 mm dishes and allowed to spread overnight. On the following day, cells were fixed in prewarmed 4% paraformaldehyde (PFA; 15170; Electron Microscopy Sciences) in PBS for 20 min. For optimal preservation of the actin cytoskeleton, 0.25% glutaraldehyde (16020; Electron Microscopy Sciences) was added to the PFA solution. For some experiments, cells were ionomycin treated as described earlier before the fixation. Then, cells were permeabilized with 0.1% Triton X-100 in PBS for 1 min. Before antibody stainings, cells were blocked with 10% calf serum in PBS for ~30 min. Primary antibodies were diluted in 1% calf serum in PBS and incubated for 1 h. Mitochondria were visualized using primary antibody against the OMM protein Tom20 (rabbit; ab78547; Abcam; 1:200). Coverslips were washed several times in PBS and incubated with secondary antibody solution for 45 min. Either anti-rabbit fluorescein (FI-1000; Vector Laboratories; 1:300) or anti-mouse Texas Red (TI-2000; Vector Laboratories; 1:300) was used as secondary antibodies. TRITC-phalloidin (1 µM; P1951; Sigma) was added with secondary antibodies to stain for actin filaments. Coverslips were washed in PBS and fixed on glass slides using ProLong Gold antifade mounting media (P36930; Invitrogen).

Phospho-MRLC (rabbit; 3671; Cell Signaling Technology; 1:50) in combination with Tom20 (mouse; sc-17764; Santa Cruz; 1:50) staining in Figure 1D was performed as described here with the

exception of sole PFA fixation, as the p-MRLC antibody was ineffective after glutaraldehyde fixation.

Endogenous NMII and Tpm staining at CIA network

For endogenous NMII localization at CIA networks (Figure 6 and Supplemental Figure S4), U2OS WT cells plated on coverslips were stimulated with either ionomycin or DMSO for 45 s. Medium was removed entirely, and cells were extracted for exactly 1 min with 0.1% Triton X-100 in PEM buffer (100 mM PIPES-Na, pH 6.9, 1 mM EGTA, 1 mM $MgCl_2$) supplemented with 4% PFA and 5 µM TRITC-phalloidin for optimal preservation of the CIA network. This extraction step was followed by a 20 min fixation in 4% PFA in PEM buffer. After being washed, coverslips were blocked with 10% calf serum in PBS for ~30 min, followed by primary antibody staining using NMII antibodies (NMIIA: #3403; NMIIB: #3404; NMIIC: #8189; all rabbit; Cell Signaling Technology; 1:50) Tpm3 (tropomyosin γ9d clone 2G10.2; mouse; 1:50) kindly provided by Peter Gunning (UNSW, Sydney, Australia) and described in Schevzov *et al.* [2005]) for 1 h at room temperature. Secondary antibody was anti-rabbit fluorescein (FI-1000; Vector Laboratories; 1:300). The actin cytoskeleton was preserved and visualized via addition of 5 µM TRITC-phalloidin in the extraction step.

Focal adhesion staining and analysis

Focal adhesions were visualized using a vinculin-reactive antibody (VIN-11-05; SAB4200729; Sigma; 1:100). TRITC-phalloidin (1 µM) was used to counterstain for the actin cytoskeleton. To reduce unspecific background staining, cells were permeabilized with 0.3% Triton X-100 in 4% PFA/PBS for 1 min before a 20 min fixation with 4% PFA/PBS. Quantifications of adhesion density (counts per 10 μm^2 cell area) and size (μm^2) were performed using ImageJ ("analyze particle" plug-in) by subtracting background signals (rolling ball radius: 20 pxl) and analyzing binary masks as illustrated in Figure 3. Data were obtained from three independent replicates and plotted as box-and-whiskers plots using Microsoft Excel.

CIA intensity measurements on fixed cells

Plan Apo (100×) images of ionomycin-stimulated cells were randomly taken on a Dragonfly 302 spinning-disk confocal microscope (Andor Technology). Exposure times and laser intensities were kept equal between various cell lines and treatments. On the TRITC-phalloidin images, a small circular area (~25 μm^2) was used to measure the mean fluorescence intensity of the calcium-induced actin network (in arbitrary units). In particular, a perinuclear, cytoplasmic area in a medial confocal plane was used for the analysis in order to avoid any signal contribution from basal stress fibers or cortical actin. These intensity values derived from ImageJ were averaged for all cells and plotted as box-and-whiskers plots using Microsoft Excel. Approximately 400 cells per cell line and treatment were analyzed from three independent experiments (Figure 4, A and B, and Supplemental Figure S3, A and B).

Live-cell imaging by confocal microscopy

Live-cell imaging was conducted in DMEM (21063-029; Life Technologies) with 25 mM D-glucose, 4 mM D-glutamine, and 25 mM HEPES, supplemented with 10% newborn calf serum (SH30118.03; HyClone). Fast time-resolution imaging was performed on a Dragonfly 302 spinning-disk confocal (Andor Technology) on a Nikon Ti-E base and equipped with an iXon Ultra 888 EMCCD camera, and a Zyla 4.2 Mpixel sCMOS camera, and a Tokai Hit stage-top incubator was used. A solid-state 405 smart diode 100-mW laser, solid-state 488 OPSL smart laser 50-mW laser, solid-state 560 OPSL smart laser 50-mW laser, and a solid-state 637 OPSL smart laser 140-mW laser were used (objective: 100 × 1.4 NA CFI Plan Apo; Nikon). Images were acquired using Fusion software (Andor Technology).

Photoactivation

To assess mitochondrial connectivity similar to past studies (Karbowski *et al.*, 2014), cells were transfected with a photoactivatable GFP probe located in the mitochondrial matrix (Figure 9, E and F). Photoactivation experiments were performed using the Dragonfly 302 spinning-disk confocal microscope (Andor Technology) driven by Fusion software (selected mode: photostimulation). GFP photoconversion was performed using a solid-state 405 smart diode 100-mW laser at 30% intensity output power (500 ms exposure). A fixed area (2 μm^2) was activated in the cell periphery containing clusters of mitochondria. Mitochondria occupied at least 90% of the activated area. Images were acquired before and 10 s after laser activation in order to avoid mitochondrial fusion contributing to GFP-signal spread over longer time periods. Quantifications of the photostimulated area were carried out in ImageJ (plug-in "measure—area") on binary masks and plotted as box-and-whiskers plots.

Measurements of calcium and actin changes in live cells

Cells were transfected with the indicated probes (GFP-F-tractin, mito-R-GECO or ER-GCaMP6-150) as described above and plated on MatTek dishes for live-cell imaging (Figures 1, A and C, 4, C–E, and 7 and Supplemental Figures S3, C–E, and S6, A–C). Cells were imaged at a single confocal slice in the medial region, approximately 2 µm above the basal surface, to avoid stress fibers. To establish baseline fluorescence, cells were first imaged in 1 ml of live-cell medium for ~1 min. Cells were then stimulated by addition of 1 ml live-cell medium containing 8 µM ionomycin (4 µM final concentration) while continuously imaging several positions at a frame rate of 15 s. Mean fluorescence intensity was calculated for each cell using the ImageJ plug-in "Time Series Analyzer V3." Fluorescence values for each time point after drug treatment were normalized to the mean baseline fluorescence (first four frames) and plotted as intensity fold change over time in seconds. Average fluorescence intensities for mitochondrial calcium or ER-calcium were determined by encircling the entire mitochondrial or ER networks, while changes in F-tractin signals were analyzed in a perinuclear region of interest (ROI) in an apical cell plane to avoid signal contribution from stress fibers. Data were plotted as intensity–time curves with SEMs for each data point or min/max intensity values graphed as box-and-whiskers plots using Microsoft Excel.

Mitochondrial length and diameter analysis

For mitochondrial length quantifications (Figure 9, A–C), fixed cells stained for the OMM using Tom20 antibody were imaged and processed following established methods (Lee *et al.*, 2016; Chakrabarti *et al.*, 2018). Briefly, maximum-intensity projections were generated from z-stacks (~15 × 0.2 µm) and background was subtracted using ImageJ (rolling ball radius: 20 pxl). One ROI of resolvable mitochondria was selected in the peripheral, spread region of the cell and analyzed using the "analyze particles" plug-in in ImageJ to obtain the number of mitochondrial fragments and the area of each fragment per ROI.

Mitochondrial diameters (Figure 8) of either perinuclear (within a distance of ~10 µm around the nucleus) or peripheral mitochondria (within a distance of ~10 µm from the nucleus to the cell edge) were measured using ImageJ plug-in "measure—length" by drawing a line across a single mitochondrion using OMM marker Tom20. At

least 300 individual mitochondria per cell line and from three independent experiments were analyzed. Note that the reported diameters here do not represent actual mitochondrial sizes due to the resolution limit of the microscope. Nonetheless, we were able to identify differences among different cell lines and conditions.

Quantification of mitochondrially associated Drp1 puncta

GFP-Drp1 knock-in cells were knocked down for individual NMII members or INF2 (Figure 10). ROIs containing mitochondria in spread, peripheral cell areas were thresholded using the same contrast settings for the Tom20 staining. Drp1 signals were first processed by background subtraction using ImageJ (rolling ball radius: 5 pxl) and then further thresholded applying equal setting parameters. Drp1 puncta with corresponding Tom20 staining were analyzed using the ImageJ "Colocalization" plug-in with the following parameters: ratio 20% (0–100%), threshold channel 1: 50 (0–255), threshold channel 2: 50 (0–255), display value (0–255): 255. Colocalized pixels were then converted to a binary mask and quantified using the "analyze particles" tool with settings as follows: size (pixel2) 0.01–infinity, circularity 0.00–1.00. Drp1:Tom20 area ratios (%) were plotted as box-and-whiskers plots using Microsoft Excel. Three independent experiments were performed.

Data processing and statistical analyses

Brightness and contrast levels were adjusted using ImageJ software. Figures were further processed and assembled with Photoshop CS4. Data analyses were carried out in ImageJ and Microsoft Excel. All statistical analyses and *p* value determinations were done using GraphPad Prism 6.01. Data sets were compared using an unpaired Student's *t* test. A probability of error of 5% ($p \leq 0.05$; * in figure panels) was considered to indicate statistical significance. **, ***, and **** indicate *p* values ≤ 0.01, ≤0.001, and ≤0.0001, respectively.

ACKNOWLEDGMENTS

We are very grateful to Jim Sellers for sending us purified NMII heavy chains, Timothy Shutt for providing the myosin IIC-GFP plasmid, Zdenek Svindrych for helpful advice on imaging, and Raj Chakrabarti for his intellectual input. We also thank Peter Gunning for providing us his self-made tropomyosin 3 antibody. This work was supported by National Institutes of Health (NIH) R35 GM122545 and R01 DK088826 to H.N.H., NIH P20 GM113132 to the Dartmouth BioMT, and Deutsche Forschungs-gemeinschaft (DFG) fellowship KA5106/1-1 to F. K. M.V.-M. acknowledges funding from the Spanish Ministry of Science and Innovation (SAF2017-87408 and PID2020-116232RB-I00) and ECRIN-M3 from AECC/AIRC/CRUK (Asociation Espanola Contra el Cancer/American International Recruitment Council/Cancer Research UK). The IBMCC (Institute of Molecular and Cell Biology of Cancer) is supported by the Programa e Apoyo a Planes Estrategicos de Investigacion de Estructuras de Investigacion de Excelencia of the Ministry of Education of the Castilla-Leon Government (CLC-2017-01). This work was also supported by NIH R35 GM119455 to A.N.K.

REFERENCES

Aguilar-Cuenca R, Llorente-González C, Chapman J, Talayero V, Garrido-Casado M, Delgado-Arévalo C, Millán-Salanova M, Shabanowitz J, Hunt D, Sellers J, *et al.* (2020). Tyrosine phosphorylation of the myosin regulatory light chain controls non-muscle myosin II assembly and function in migrating cells. Curr Biol 30, 2446–2458.e6.

Almutawa W, Smith C, Sabouny R, Smit R, Zhao T, Wong R, Lee-Glover L, Desrochers-Goyette J, Ilamathi H, Suchowersky O, *et al.* (2019). The R941L mutation in MYH14 disrupts mitochondrial fission and associates with peripheral neuropathy. EBioMedicine 45, 379–392.

Andrés-Delgado L, Antón OM, Madrid R, Byrne JA, Alonso MA (2010). Formin INF2 regulates MAL-mediated transport of Lck to the plasma membrane of human T lymphocytes. Blood 116, 5919–5929.

Bartolini F, Andres-Delgado L, Qu X, Nik S, Ramalingam N, Kremer L, Alonso MA, Gundersen GG (2016). An mDia1-INF2 formin activation cascade facilitated by IQGAP1 regulates stable microtubules in migrating cells. Mol Biol Cell 27, 1797–1808.

Bayraktar S, Nehrig J, Menis E, Karli K, Janning A, Struk T, Halbritter J, Michgehl U, Krahn M, Schuberth C, *et al.* (2020). A deregulated stress response underlies distinct INF2-associated disease profiles. J Am Soc Nephrol 31, 1296–1313.

Beach J, Bruun K, Shao L, Li D, Swider Z, Remmert K, Zhang Y, Conti M, Adelstein R, Rusan N, *et al.* (2017). Actin dynamics and competition for myosin monomer govern the sequential amplification of myosin filaments. Nat Cell Biol 19, 85–93.

Beach JR, Shao L, Remmert K, Li D, Betzig E, Hammer JA (2014). Nonmuscle myosin II isoforms coassemble in living cells. Curr Biol 24, 1160–1166.

Billington N, Wang A, Mao J, Adelstein RS, Sellers JR (2013). Characterization of three full-length human nonmuscle myosin II paralogs. J Biol Chem 288, 33398–33410.

Bird JE, Takagi Y, Billington N, Strub MP, Sellers JR, Friedman TB (2014). Chaperone-enhanced purification of unconventional myosin 15, a molecular motor specialized for stereocilia protein trafficking. Proc Natl Acad Sci USA 111, 12390–12395.

Boyer O, Nevo F, Plaisier E, Funalot B, Gribouval O, Benoit G, Cong E, Arrondel C, Tete M, Montjean R, *et al.* (2011). INF2 mutations in Charcot–Marie–Tooth disease with glomerulopathy. N Engl J Med 365, 2377–2388.

Brown EJ, Schlöndorff JS, Becker DJ, Tsukaguchi H, Uscinski AL, Higgs HN, Henderson JM, Pollak MR (2010). Mutations in the formin gene INF2 cause focal segmental glomerulosclerosis. Nat Genet 42, 72–76.

Chakrabarti R, Ji WK, Stan RV, Sanz JJ, Ryan TA, Higgs HN (2018). INF2-mediated actin polymerization at the ER stimulates mitochondrial calcium uptake, inner membrane constriction, and division. J Cell Biol 217, 251–268.

Chang CW, Kumar S (2015). Differential contributions of nonmuscle myosin II isoforms and functional domains to stress fiber mechanics. Sci Rep 5, 13736.

Chhabra ES, Ramabhadran V, Gerber SA, Higgs HN (2009). INF2 is an endoplasmic reticulum-associated formin protein. J Cell Sci 122, 1430–1440.

Chinowsky CR, Pinette JA, Meenderink LM, Lau KS, Tyska MJ (2020). Nonmuscle myosin-2 contractility-dependent actin turnover limits the length of epithelial microvilli. Mol Biol Cell 31, 2803–2815.

Cho B, Cho H, Jo Y, Kim H, Song M, Moon C, Kim H, Kim K, Sesaki H, Rhyu I, *et al.* (2017). Constriction of the mitochondrial inner compartment is a priming event for mitochondrial division. Nat Commun 8, 15754.

Collins TJ (2002). Mitochondria are morphologically and functionally heterogeneous within cells. EMBO J 21, 1616–1627.

de Juan-Sanz J, Holt GT, Schreiter ER, de Juan F, Kim DS, Ryan TA (2017). Axonal endoplasmic reticulum Ca2+ content controls release probability in CNS nerve terminals. Neuron 93, 867–881.e6.

Dulyaninova NG, Bresnick AR (2013). The heavy chain has its day: regulation of myosin-II assembly. Bioarchitecture 3, 77–85.

Eng JK, Jahan TA, Hoopmann MR (2013). Comet: an open-source MS/MS sequence database search tool. Proteomics 13, 22–24.

Even-Ram S, Doyle AD, Conti MA, Matsumoto K, Adelstein RS, Yamada KM (2007). Myosin IIA regulates cell motility and actomyosin-microtubule crosstalk. Nat Cell Biol 9, 299–309.

Fenix AM, Taneja N, Buttler CA, Lewis J, van Engelenburg SB, Ohi R, Burnette DT (2016). Expansion and concatenation of nonmuscle myosin IIA filaments drive cellular contractile system formation during interphase and mitosis. Mol Biol Cell 27, 1465–1478.

Fernández-Barrera J, Bernabé-Rubio M, Casares-Arias J, Rangel L, Fernández-Martín L, Correas I, Alonso MA (2018). The actin-MRTF-SRF transcriptional circuit controls tubulin acetylation via α-TAT1 gene expression. J Cell Biol 217, 929–944.

Fu X, Zhang L, Jin Y, Sun X, Zhang A, Wen Z, Zhou Y, Xia M, Gao J (2016). Loss of Myh14 increases susceptibility to noise-induced hearing loss in CBA/CaJ mice. Neural Plast 2016, 6720420.

Fung TS, Ji WK, Higgs HN, Chakrabarti R (2019). Two distinct actin filament populations have effects on mitochondria, with differences in stimuli and assembly factors. J Cell Sci 132, jcs234435.

Gaillard J, Ramabhadran V, Neumanne E, Gurel P, Blanchoin L, Vantard M, Higgs HN (2011). Differential interactions of the formins INF2, mDia1,and mDia2 with microtubules. Mol Biol Cell 22, 4575–4587.

Golomb E, Ma X, Jana SS, Preston YA, Kawamoto S, Shoham NG, Goldin E, Conti MA, Sellers JR, Adelstein RS (2004). Identification and characterization of nonmuscle myosin II-C, a new member of the myosin II family. J Biol Chem 279, 2800–2808.
Heissler SM, Sellers JR (2015). Four things to know about myosin light chains as reporters for non-muscle myosin-2 dynamics in live cells. Cytoskeleton 72, 65–70.
Hu S, Dasbiswas K, Guo Z, Tee YH, Thiagarajan V, Hersen P, Chew TL, Safran SA, Zaidel-Bar R, Bershadsky AD (2017). Long-range self-organization of cytoskeletal myosin II filament stacks. Nat Cell Biol 19, 133–141.
Ji WK, Chakrabarti R, Fan X, Schoenfeld L, Strack S, Higgs HN (2017). Receptor-mediated Drp1 oligomerization on endoplasmic reticulum. J Cell Biol 216, 4123–4139.
Ji WK, Hatch AL, Merrill RA, Strack S, Higgs HN (2015). Actin filaments target the oligomeric maturation of the dynamin GTPase Drp1 to mitochondrial fission sites. eLife 4, e11553.
Johnson HW, Schell MJ (2009). Neuronal IP3 3-kinase is an F-actin-bundling protein: role in dendritic targeting and regulation of spine morphology. Mol Biol Cell 20, 5166–5180.
Karbowski M, Cleland MM, Roelofs BA (2014). Photoactivatable green fluorescent protein-based visualization and quantification of mitochondrial fusion and mitochondrial network complexity in living cells. Methods Enzymol 547, 57–73.
Kim BJ, Kim AR, Han JH, Lee C, Oh DY, Choi BY (2017). Discovery of MYH14 as an important and unique deafness gene causing prelingually severe autosomal dominant nonsyndromic hearing loss. J Gene Med 19, 770–776.
Korobova F, Gauvin TJ, Higgs HN (2014). A role for myosin II in mammalian mitochondrial fission. Curr Biol 24, 409–414.
Korobova F, Ramabhadran V, Higgs HN (2013). An actin-dependent step in mitochondrial fission mediated by the ER-associated formin INF2. Science 339, 464–467.
Kraus F, Roy K, Pucadyil TJ, Ryan MT (2021). Function and regulation of the divisome for mitochondrial fission. Nature 590, 57–66.
Kuragano M, Uyeda TQP, Kamijo K, Murakami Y, Takahashi M, Wang YL (2018). Different contributions of nonmuscle myosin IIA and IIB to the organization of stress fiber subtypes in fibroblasts. Mol Biol Cell 29, 911–922.
Labat-de-Hoz L, Alonso MA (2020). The formin INF2 in disease: progress from 10 years of research. Cell Mol Life Sci 77, 4581–4600.
Lamm KYB, Johnson ML, Phillips JB, Muntifering MB, James JM, Jones HN, Redline RW, Rokas A, Muglia LJ (2018). Inverted formin 2 regulates intracellular trafficking, placentation, and pregnancy outcome. eLife 7. e31150.
Laplante C, Huang F, Tebbs IR, Bewersdorf J, Pollard TD (2016). Molecular organization of cytokinesis nodes and contractile rings by super-resolution fluorescence microscopy of live fission yeast. Proc Natl Acad Sci USA 113, E5876–E5885.
Laporte D, Coffman VC, Lee IJ, Wu JQ (2011). Assembly and architecture of precursor nodes during fission yeast cytokinesis. J Cell Biol 192, 1005–1021.
Lee JE, Westrate LM, Wu H, Page C, Voeltz GK (2016). Multiple dynamin family members collaborate to drive mitochondrial division. Nature 540, 139–143.
Limouze J, Straight AF, Mitchison T, Sellers JR (2004). Specificity of blebbistatin, an inhibitor of myosin II. J Muscle Res Cell Motil 25, 337–341.
Lin S, Huang C, Gunda V, Sun J, Chellappan S, Li Z, Izumi V, Fang B, Koomen J, Singh P, *et al.* (2019). Fascin controls metastatic colonization and mitochondrial oxidative phosphorylation by remodeling mitochondrial actin filaments. Cell Rep 28, 2824–2836.e8.
Lu Z, Ma XN, Zhang HM, Ji HH, Ding H, Zhang J, Luo D, Sun Y, Li XD (2014). Mouse myosin-19 is a plus-end-directed, high-duty ratio molecular motor. J Biol Chem 289, 18535–18548.
Ma X, Adelstein RS (2014). The role of vertebrate nonmuscle myosin II in development and human disease. Bioarchitecture 4, 88–102.
Ma X, Jana SS, Conti MA, Kawamoto S, Claycomb WC, Adelstein RS (2010). Ablation of nonmuscle myosin II-B and II-C reveals a role for nonmuscle myosin II in cardiac myocyte karyokinesis. Mol Biol Cell 21, 3952–3962.
Madrid R, Aranda J, Rodriguez-Fraticelli A, Ventimiglia L, Andres-Delgado L, Shehata M, Fanayan S, Shahheydari H, Gomez S, Jimenez A, *et al.* (2010). The formin INF2 regulates basolateral-to-apical transcytosis and lumen formation in association with Cdc42 and MAL2. Dev Cell 18, 814–827.
Manor U, Bartholomew S, Golani G, Christenson E, Kozlov M, Higgs H, Spudich J, Lippincott-Schwartz J (2015). A mitochondria-anchored isoform of the actin-nucleating spire protein regulates mitochondrial division. eLife 4, e08828.
McDonald NA, Lind AL, Smith SE, Li R, Gould KL (2017). Nanoscale architecture of the Schizosaccharomyces pombe contractile ring. eLife 6, e28865.
Mu A, Fung TS, Francomacaro LM, Huynh T, Kotila T, Svindrych Z, Higgs HN (2020). Regulation of INF2-mediated actin polymerization through site-specific lysine acetylation of actin itself. Proc Natl Acad Sci USA 117, 439–447.
Mu A, Fung TS, Kettenbach AN, Chakrabarti R, Higgs HN (2019). A complex containing lysine-acetylated actin inhibits the formin INF2. Nat Cell Biol 21, 592–602.
Ramabhadran V, Korobova F, Rahme GJ, Higgs HN (2011). Splice variant-specific cellular function of the formin INF2 in maintenance of Golgi architecture. Mol Biol Cell 22, 4822–4833.
Rauscher A, Gyimesi M, Kovács M, Málnási-Csizmadia A (2018). Targeting myosin by blebbistatin derivatives: optimization and pharmacological potential. Trends Biochem Sci 43, 700–713.
Schevzov G, Vrhovski B, Bryce NS, Elmir S, Qiu MR, O'Neill GM, Yang N, Verrills NM, Kavallaris M, Gunning PW (2005). Tissue-specific tropomyosin isoform composition. J Histochem Cytochem 53, 557–570.
Sellers JR, Heissler SM (2019). Nonmuscle myosin-2 isoforms. Curr Biol 29, R275–R278.
Shao X, Li Q, Mogilner A, Bershadsky AD, Shivashankar GV (2015). Mechanical stimulation induces formin-dependent assembly of a perinuclear actin rim. Proc Natl Acad Sci USA 112, E2595–E2601.
Shutova MS, Asokan SB, Talwar S, Assoian RK, Bear JE, Svitkina TM (2017). Self-sorting of nonmuscle myosins IIA and IIB polarizes the cytoskeleton and modulates cell motility. J Cell Biol 216, 2877–2889.
Shutova MS, Spessott WA, Giraudo CG, Svitkina T (2014). Endogenous species of mammalian nonmuscle myosin IIA and IIB include activated monomers and heteropolymers. Curr Biol 24, 1958–1968.
Takeuchi Y, Narumi R, Akiyama R, Vitiello E, Shirai T, Tanimura N, Kuromiya K, Ishikawa S, Kajita M, Tada M, *et al.* (2020). Calcium wave promotes cell extrusion. Curr Biol 30, 670–681.e6.
Taneja N, Bersi MR, Baillargeon SM, Fenix AM, Cooper JA, Ohi R, Gama V, Merryman WD, Burnette DT (2020). Precise tuning of cortical contractility regulates cell shape during cytokinesis. Cell Rep 31, 107477.
Taneja N, Burnette DT (2019). Myosin IIA drives membrane bleb retraction. Mol Biol Cell 30, 1051–1059.
Valm AM, Cohen S, Legant WR, Melunis J, Hershberg U, Wait E, Cohen AR, Davidson MW, Betzig E, Lippincott-Schwartz J (2017). Applying systems-level spectral imaging and analysis to reveal the organelle interactome. Nature 546, 162–167.
Valot B, Langella O, Nano E, Zivy M (2011). MassChroQ: a versatile tool for mass spectrometry quantification. Proteomics 11, 3572–3577.
Vicente-Manzanares M, Koach MA, Whitmore L, Lamers ML, Horwitz AF (2008). Segregation and activation of myosin IIB creates a rear in migrating cells. J Cell Biol 183, 543–554.
Vicente-Manzanares M, Zareno J, Whitmore L, Choi CK, Horwitz AF (2007). Regulation of protrusion, adhesion dynamics, and polarity by myosins IIA and IIB in migrating cells. J Cell Biol 176, 573–580.
Wales P, Schuberth C, Aufschnaiter R, Fels J, Garcia-Aguilar I, Janning A, Dlugos C, Schäfer-Herte M, Klingner C, Wälte M, *et al.* (2016). Calcium-mediated actin reset (CaAR) mediates acute cell adaptations. eLife 5, e19850.
Wang Y, Sherrard A, Zhao B, Melak M, Trautwein J, Kleinschnitz EM, Tsopoulidis N, Fackler OT, Schwan C, Grosse R (2019). GPCR-induced calcium transients trigger nuclear actin assembly for chromatin dynamics. Nat Commun 10, 5271.
Weißenbruch K, Grewe J, Hippler M, Fladung M, Tremmel M, Stricker K, Schwarz US, Bastmeyer M (2021). Distinct roles of nonmuscle myosin II isoforms for establishing tension and elasticity during cell morphodynamics. eLife 10, e71888.
Wu J, Prole D, Shen Y, Lin Z, Gnanasekaran A, Liu Y, Chen L, Zhou H, Chen S, Usachev Y, *et al.* (2014). Red fluorescent genetically encoded Ca2+ indicators for use in mitochondria and endoplasmic reticulum. Biochem J 464, 13–22.
Xu XS, Lee E, Chen T, Kuczmarski E, Chisholm RL, Knecht DA (2001). During multicellular migration, myosin II serves a structural role independent of its motor function. Dev Biol 232, 255–264.
Yamamoto K, Otomo K, Nemoto T, Ishihara S, Haga H, Nagasaki A, Murakami Y, Takahashi M (2019). Differential contributions of nonmuscle myosin IIA and IIB to cytokinesis in human immortalized fibroblasts. Exp Cell Res 376, 67–76.
Yang C, Svitkina TM (2019). Ultrastructure and dynamics of the actin–myosin II cytoskeleton during mitochondrial fission. Nat Cell Biol 21, 603–613.